1

2

Bulk Nanostructured Materials

4

C. C. Koch[1*], T. G. Langdon[2,3], E. J. Lavernia[4]

1. Department of Materials Science and Engineering, North Carolina State University, Raleigh, NC 27695, USA

2. Departments of Aerospace & Mechanical Engineering and Materials Science, University of Southern California, Los Angeles, CA 90089, USA

3. Materials Research Group, Faculty of Engineering and the Environment, University of Southampton, SO17 1BJ, UK

4. Department of Chemical Engineering and Materials Science, University of California, Irvine, Irvine, CA 92697, USA

14

*Corresponding author: email: carl_koch@ncsu.edu
16

Abstract

This paper will address three topics of importance to bulk nanostructured materials. Bulk nanostructured materials are defined as bulk solids with nanoscale or partly nanoscale microstructures. This category of nanostructured materials has historical roots going back many decades but has relatively recent focus due to new discoveries of unique properties of some nanoscale materials. Bulk nanostructured materials are prepared by a variety of severe plastic deformation methods, and these will be reviewed. Powder processing to prepare bulk nanostructured materials requires that the powders be consolidated by typically combinations of pressure and temperature, the latter leading to coarsening of the microstructure. The thermal stability of nanostructured materials will also be discussed. An example of bringing nanostructured materials to applications as structural materials will be described in terms of the cryomilling of powders and their consolidation.

29

I. INTRODUCTION

Bulk nanostructured materials are defined as bulk solids with nanoscale or partly nanoscale microstructures. This category of nanostructured materials has historical roots going back many decades but has relatively recent focus due to new discoveries of unique properties of some nanoscale materials.

Early in the last century, when "microstructures" were revealed primarily with the optical microscope, it was recognized that refined microstructures, for example, small grain sizes, often provided attractive properties such as increased strength and toughness in structural materials. A classic example of property enhancement due to a refined microstructure- with features too small to resolve with the optical microscope- was age hardening of aluminum alloys.

The field of nanocrystalline (or nanostructured) materials as a major identifiable activity in modern materials science results to a large degree from the work in the 1980s of Gleiter and co-workers [1] who synthesized nanoscale (<100 nm) grain size materials by the *in situ* consolidation of nanoscale atomic clusters. These nanostructured materials exhibited dramatically improved – or different - properties from conventional grain size (> 1 μm) polycrystalline or single crystal materials of the same chemical composition. This is the stimulus for the tremendous appeal of these materials.

There are a number of processing methods to produce bulk nanostructured materials. These include the inert gas condensation method pioneered by Gleiter [1], electrodeposition [2], crystallization of amorphous precursors [3], severe plastic deformation methods [4], or the consolidation of nanoscale powder precursors [5]. The nanoscale powder precursors may be nanoscale powders produced by a variety of chemical methods [6] or powders which are micron

52   or tens of microns in size but with a nanoscale grain size produced by ball milling of powders.

53   The methods to be emphasized in this short review will be those that involve either severe plastic

54   deformation of bulk materials, or the severe plastic deformation (mechanical attrition) of

55   powders followed by consolidation into bulk.

56   The paper will begin with a review of severe plastic deformation techniques. This will be

57   followed by a consideration of the problem of the stabilization of nanoscale grain size in

58   powders during their consolidation which involves elevated temperatures. The concluding

59   section will give an example of aluminum alloys prepared by mechanical alloying and

60   consolidated by conventional commercial processing such as extrusion. Their grain size is

61   stabilized by nanoscale precipitates of oxides and nitrides. A summary will discuss the existing

62   or potential applications of bulk nanostructured materials.

63

64   **II. BULK   NANOSTRUCTURED   MATERIALS   BY   SEVERE   PLASTIC**

65   **DEFORMATION**

66   Metal processing is generally based on conventional procedures, such as rolling, extrusion

67   and drawing, in which one of the dimensions of the work-piece is significantly reduced during

68   the processing operation.   Nevertheless, alternative procedures are now available where

69   exceptionally high strains may be imposed without incurring any major changes in the overall

70   dimensions of the samples. This type of processing relates to the application of severe plastic

71   deformation (SPD) and the processing has been defined formally as "any method of metal

72   forming under an extensive hydrostatic pressure that may be used to impose a very high strain on

73   a bulk solid without the introduction of any significant change in the overall dimensions of the

74   sample" [7].   In practice, SPD processing provides a unique opportunity for achieving

3

75 exceptional grain refinement, typically to the sub-micrometer or even the nanometer level, and

76 thereby it provides the potential for obtaining superior properties that cannot be achieved using

77 more conventional techniques.

78 The following section provides a brief historical review of the development of SPD processing

79 leading up to the recognition that these procedures may be used to produce exceptionally small

80 grain sizes in metals and the following sections describe the more recent developments of these

81 procedures and the potential for attaining unusual and useful properties in bulk metallic solids.

82 *A. The Development of SPD as a Processing Tool*

83 SPD processing is generally considered a very new metallurgical tool but in fact

84 comprehensive analyses have shown that the general principles of SPD were employed over

85 2000 years ago in ancient China [8, 9]. Thus, in the Han dynasty in China around 200 BC a new

86 and effective forging technique was developed for the fabrication of steel for use in swords. This

87 technique consisted of repetitively forging and folding a metal to produce very high strength as

88 in the famous Bai-Lian steels and later a similar technique was used in the processing ultrahigh

89 carbon Wootz steels in ancient India [10] and then Damascus steels in the Middle East [11].

90 Despite the remarkable success of this approach in achieving high strengths, these procedures

91 were followed by medieval artisans without any formal understanding of the fundamental

92 scientific principles associated with the processing.

93 The first scientific approach to SPD processing may be traced to the work of P.W. Bridgman

94 at Harvard University dating from the 1930's onwards [12]. Bridgman single-handedly

95 investigated the processing of metals using a combination of compression and torsional straining

96 and thus he essentially introduced the procedure that is known today as High-Pressure Torsion

97 (HPT). Subsequently, in 1946, Bridgman received the Nobel Prize in Physics for his work on

4

98   the effects of high pressures on bulk metals. Over a period of many years, Bridgman amassed a

99   large volume of data on the applications of high pressures to a remarkably wide range of

100   materials and this work was summarized in a book published in 1952 [13] and more recently in a

101   comprehensive review article [14]. Following Bridgman, the principles of HPT were further

102   developed extensively by scientists working in the Soviet Union [15]. A second important

103   development occurred, also in the Soviet Union, when Segal and co-workers [16] processed

104   metals using the procedure that is now known as Equal-Channel Angular Pressing (ECAP).

105   Nevertheless, all of this work on HPT and ECAP was devoted exclusively to examining the

106   experimental parameters associated with the development of these techniques in the production

107   of high-strength materials and there was no reference to the underlying microstructure that is

108   now recognized to play a major role in determining the fundamental physical properties of the

109   material.

110   In practice, the evolution of SPD processing through microstructural analysis required the

111   introduction of sophisticated analytical tools such as high-resolution transmission electron

112   microscopy and, more recently, electron backscatter diffraction. The first recognition of the

113   importance of these microstructural effects again occurred in the Soviet Union with the work of

114   Valiev and his colleagues in the late 1980's [17]. These investigations provided the first

115   demonstration that it was possible to achieve remarkable grain refinement in many metallic

116   alloys through the use of SPD processing. For example, a grain size of ~0.3 μm was reported in

117   a superplastic Al-4% Cu-0.5% Zr alloy [17] even though in western countries at this time the

118   smallest attainable grain size in this alloy was generally considered to be about ~3-5 μm [18].

119   Later detailed reports of this work in the western literature [19, 20] provided the impetus for the

120 subsequent rapid expansion of these SPD processing techniques to many laboratories around the

121 world.

122 In addition to ECAP and HPT, several other SPD procedures have been developed which

123 may be used effectively to process metals without incurring any changes in the overall

124 dimensions and providing the potential for achieving excellent grain refinement. Examples of

125 these methods include accumulative roll bonding (ARB) [21.22], multi-directional forging

126 [23,24], multi-axial compression(MAC) [25,26], cyclic extrusion and compression [27,28],

127 repetitive corrugation and straightening (RCS) [29,30] and twist extrusion [31,32]. Nevertheless,

128 ECAP and HPT are the two SPD procedures used most frequently in modern processing [33]

129 primarily because ECAP is simple to conduct in any laboratory and may be used to provide

130 reasonably large samples and HPT leads to an optimum refined microstructure. For example, in

131 comparisons between HPT and ECAP it was shown that HPT produces smaller grains [34, 35]

132 and a larger fraction of grain boundaries having high angles of misorientation [36]. The

133 superiority of HPT in producing exceptional grain refinement was also demonstrated in direct

134 comparisons with the alternative procedures of MAC [37] and RCS [38].

135 *B. Characteristics of Bulk Nanostructured Materials Produced Using Conventional SPD*

136 Processing by ECAP is a procedure where a sample, in the form of a bar or rod, is pressed

137 through a die constrained within a channel which is bent through an abrupt angle within the die

138 [39]. It has been shown that the strain imposed in a single pass in ECAP is dependent primarily

139 upon the angle subtended internally by the channel and also to a minor extent by the outer arc of

140 curvature where the two parts of the channel intersect. Thus, for a channel angle of 90° and a

141 typical outer arc of curvature of ~20° the imposed strain is close to ~1 on each pass [40].

142 Repetitive pressings may be undertaken to impose even higher strains and then the orientations

6

143 of the samples in each pass become critical because these orientations affect the slip systems

144 within the specimen. For optimum conditions, samples in ECAP are generally processed using

145 route B_C in which the billet is rotated in the same sense by 90° about the longitudinal axis

146 between each pass [41].

147 Numerous reports are now available documenting the microstructures that may be achieved

148 using ECAP [42,43] but a comprehensive evaluation was presented where high purity (99.99%)

149 aluminum was processed by ECAP at room temperature (RT) for up to 12 passes using a 90° die

150 and then the samples were examined using orientation imagining microscopy (OIM) [44]. The

151 results are shown in Fig. 1 where the grain colors relate to the orientation of each grain as shown

152 in the unit triangle. In these images, high-angle grain boundaries (HAGBs) are defined as

153 boundaries having misorientations of more than 15° and low-angle grain boundaries (LAGBs)

154 have misorientations between 2° and 15°. Fig. 1(a) shows the initial unprocessed microstructure

155 where the grain size was ~1 µm and Figs. 1(b)–(g) show the microstructures after processing by

156 ECAP at RT through 1 to 12 passes: it is important to note that (c)-(f) have similar

157 magnifications but a higher magnification is used in Fig. 1(g) to show more fully the final grain

158 structure. Inspection of these images shows that the grain structure evolves from elongated

159 subgrains to reasonably equiaxed ultrafine grains over 1 to 4 passes and thereafter the average

160 grain size and the grain aspect ratio remain reasonably constant up to 12 passes with a final grain

161 size of ~1.2 µm. Measurements of the boundary misorientations showed the HAGBs accounted

162 for ~74% of all boundaries after 12 passes and there was an increasingly weaker texture after

163 processing through higher numbers of passes. Hardness measurements taken after ECAP

164 processing have demonstrated that there is a high degree of homogeneity in these measurements

165 both on cross-sectional planes [45] and longitudinal planes [46] although there generally remains

166   a very narrow region of lower hardness, having a width of ~0.5 mm, adjacent to the lower

167   surface. Thus, processing by ECAP is an excellent procedure for achieving very significant

168   grain refinement and a very high degree of microstructural homogeneity. Furthermore, although

169   the results in Fig. 1 relate to high-purity Al where the minimum grain size is ~1.2 μm, very

170   similar results were reported also in an Al-1% Mg solid solution alloy where the minimum grain

171   size was ~700 nm [47].
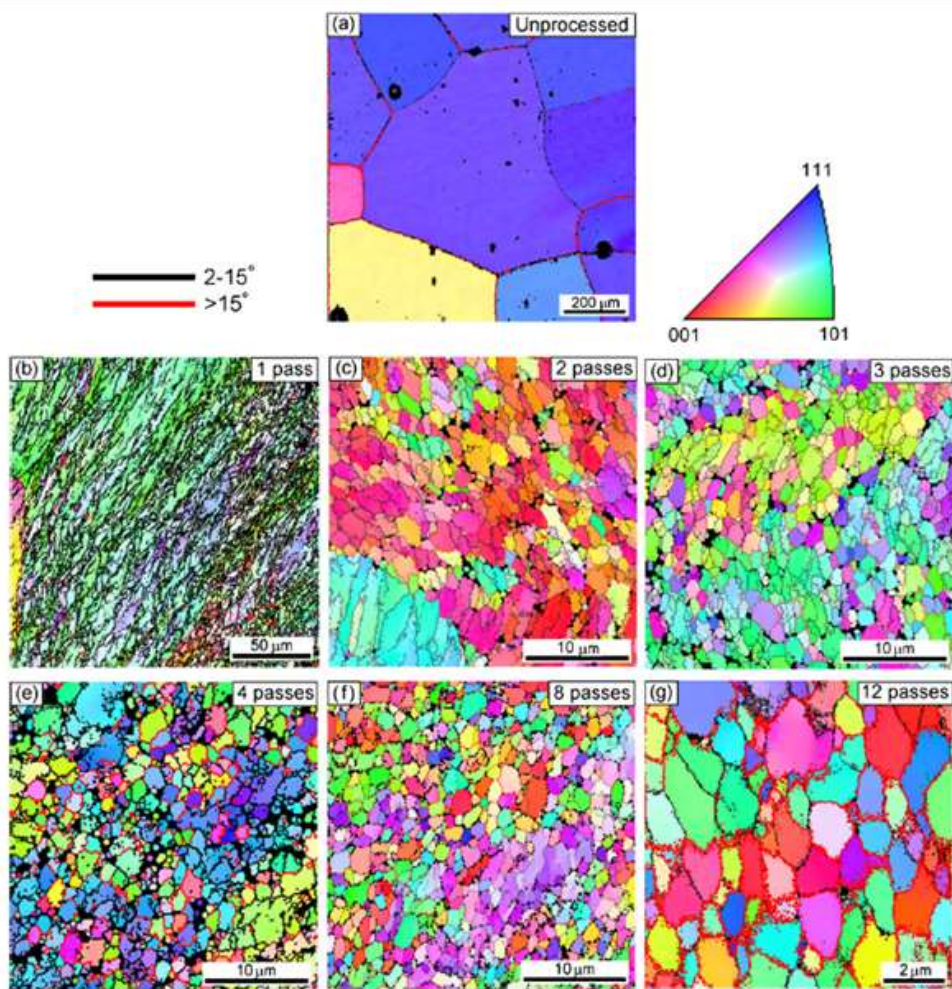
172

173   Figure 1 OIM images for high purity aluminum in (a) the initial unprocessed condition and after
174   ECAP through (b) 1, (c) 2, (d) 3, (e) 4, (f) 8 and (g) 12 passes using route BC at RT: the grain
175   colors correspond to the orientations in the unit triangle. Reprinted with permission from
176   reference [44].

177

8

178   Processing by HPT is very different from ECAP because it generally uses a sample in the

179   form of a thin disk which is placed between two large anvils and subjected to a high applied

180   pressure and concurrent torsional straining [48]. Furthermore, processing by HPT leads to an

181   equivalent von Mises strain imposed on the disk, ε_{eq}, which is given by a relationship of the

182   form [49,50]:

183        $$\varepsilon_{eq} = \frac{2\pi Nr}{h\sqrt{3}} \hspace{5cm} (1)$$

184   where r and h are the radius and height (or thickness) of the disk, respectively and N represents

185   the number of HPT turns. Inspection of Eq. (1) shows that the imposed strain varies across the

186   disk with a maximum value at the outer edge and a strain equal to zero where $r = 0$ at the center

187   of the disk. Thus, it is reasonable to anticipate that the microstructure and measurements of the

188   microhardness will vary significantly across the HPT disk and this suggests that it may be

189   impossible to achieve a high degree of homogeneity. In practice, however, early +experiments

190   showed that it was both possible to achieve a reasonable level of homogeneity after a sufficiently

191   large number of turns [51] and also that the degree of inhomogeneity in HPT disks decreases

192   with increasing strain [52]. It was demonstrated by theoretical analysis that the development of

193   homogeneity may be anticipated based on an application of strain gradient plasticity modeling

194   [53] and detailed experiments showed that excellent hardness homogeneity may be achieved

195   throughout the disks at high strains by measuring the hardness values on sectional planes after

196   straining [54]. The evolution towards a saturation microstructure at high strains may occur in

197   different ways depending upon the extent of any recovery and the precise role of strengthening

198   and weakening [55]. This evolution was examined in a recent comprehensive review which

199   summarizes HPT data for a large number of materials [56].

Cu-0.1 wt.% Zr
HPT: 6.0 GPa, RT

200
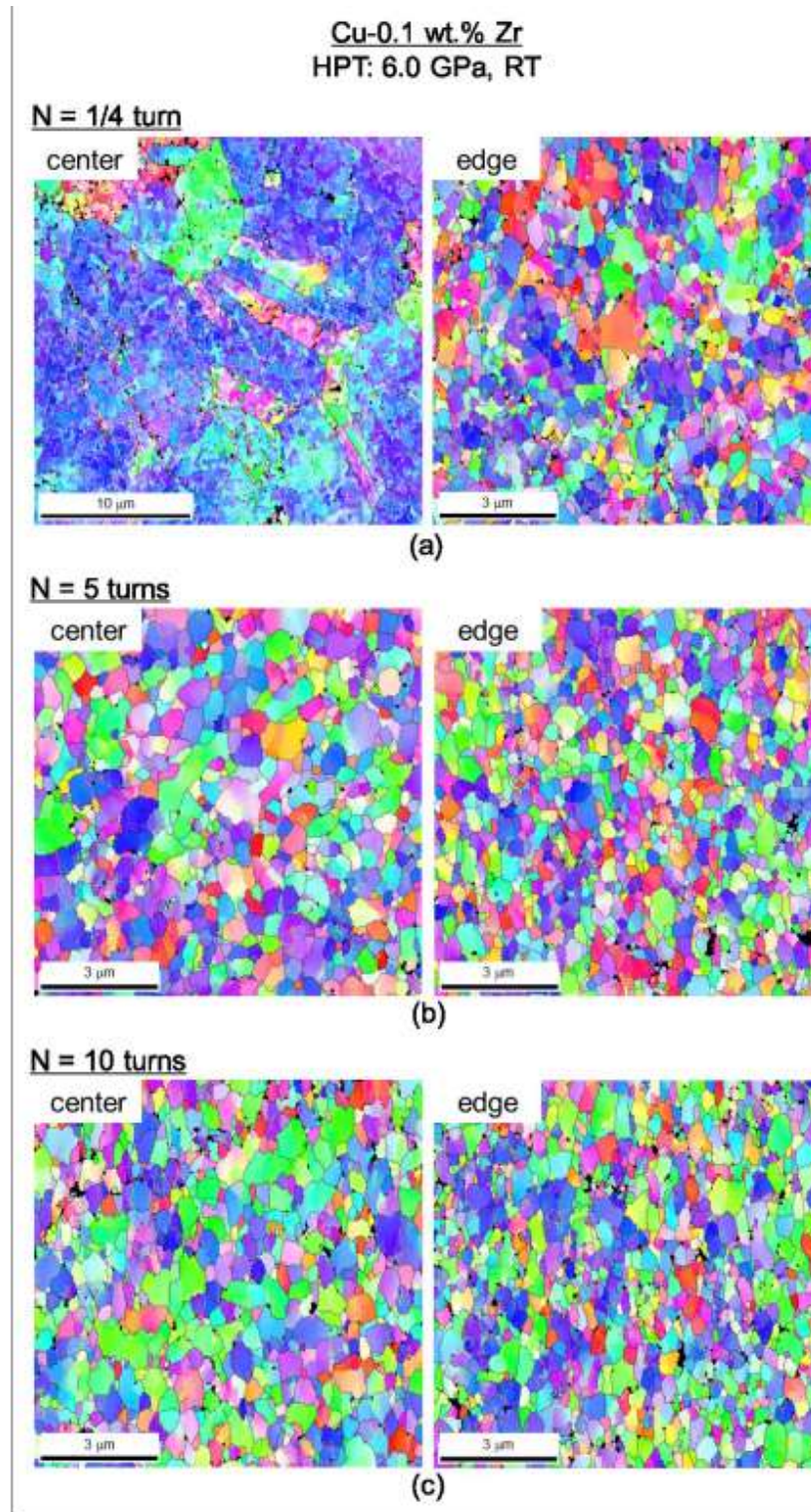
Figure 2. EBSD orientation images of Cu-0.1% Zr disks processed by HPT for (a) 1/4 turn, (b) 5 turns and (c) 10 turns: the columns display images from the center of the disk (on left) and at the edge of the disk (on right). Reprinted with permission from reference [57].

204

205   Figure 2 shows electron backscatter diffraction (EBSD) images of the microstructural

206   evolution in a Cu-0.1% Zr alloy processed by HPT at RT under an applied pressure of 6.0 GPa

207   where the three rows relate to 1/4 , 5 and 10 turns and the two columns correspond to the

208   approximate center of the disk on the left and near the edge of the disk on the right, respectively

209   [57]. The grain size initially was ~20 μm but the images show the occurrence of very extensive

210   grain refinement during HPT processing such that after 10 turns the measured grain sizes were

211   ~270 and ~230 nm at the center and near the edge, respectively.

212   *C. Recent Developments in Processing by ECAP*

213   Processing by ECAP can be achieved easily in the laboratory but it is a labor-intensive

214   process because of the need to press the same billet through the die a number of times.

215   Accordingly, much attention has been devoted to developing other approaches that may have

216   more use in industrial applications [58-60]. A simple procedure to avoid the need for multiple

217   pressings in ECAP is to construct a multi-pass die in which a high strain is imposed in a single

218   pass [61]. This procedure works well and produces results which are essentially identical to

219   those achieved using a series of separate passes through a conventional ECAP die [61] but

220   nevertheless it has the disadvantage that it exposes the die to large loads which require special

221   technical solutions. A second problem in conventional ECAP is that is produces billets having

222   gross distortions at either end and this leads to a wastage of material of an estimated order of

223   ~30-50% [62]. In practice, this wastage may be avoided by using an ECAP die having two

224   parallel channels since the second channel restores the original shape of the billet and effectively

225   eliminates the end effects [62]. Accordingly, this approach has been used successfully in several

226   investigations [63-65].

227   The most effective procedure for improving on conventional ECAP, and for producing long

228   samples with lengths of up to >1 m, is to combine ECAP with the Conform process which was

229   developed over forty years ago in the atomic energy industry in the U.K. [66,67]. Basically, the

230   Conform process permits the continuous extrusion forming of wires using the frictional forces

231   between a wire introduced from a continuous roll and a grove machined into a rotating wheel.

232   This leads to a transition from an initial circular cross-section of the wire to a rectangular cross-

233   section and, by inserting an ECAP step in the form of an abrupt abutment which displaces the

234   wire through 90° at the exit channel, it is feasible to impose a strain of ~1 as in conventional

235   ECAP and to achieve significant grain refinement. Furthermore, unlike conventional ECAP, the

236   ECAP-Conform process may be used in the production of long rods which cannot be processed

237   using conventional ECAP dies. This ECAP-Conform process has been used successfully on

238   several different metals [68-75] and it is illustrated schematically in Fig. 3 [72]. An example of

239   the grain refinement achieved using this procedure is given by results on an Al-6061 alloy where

240   an initial equiaxed grain size of ~350 μm was reduced to elongated grains with lengths of 1.5 μm

241   and widths of ~700 nm after a single pass through the ECAP-Conform die and to lengths of ~1.2

242   μm and widths of ~150 nm after 4 passes [72].

243
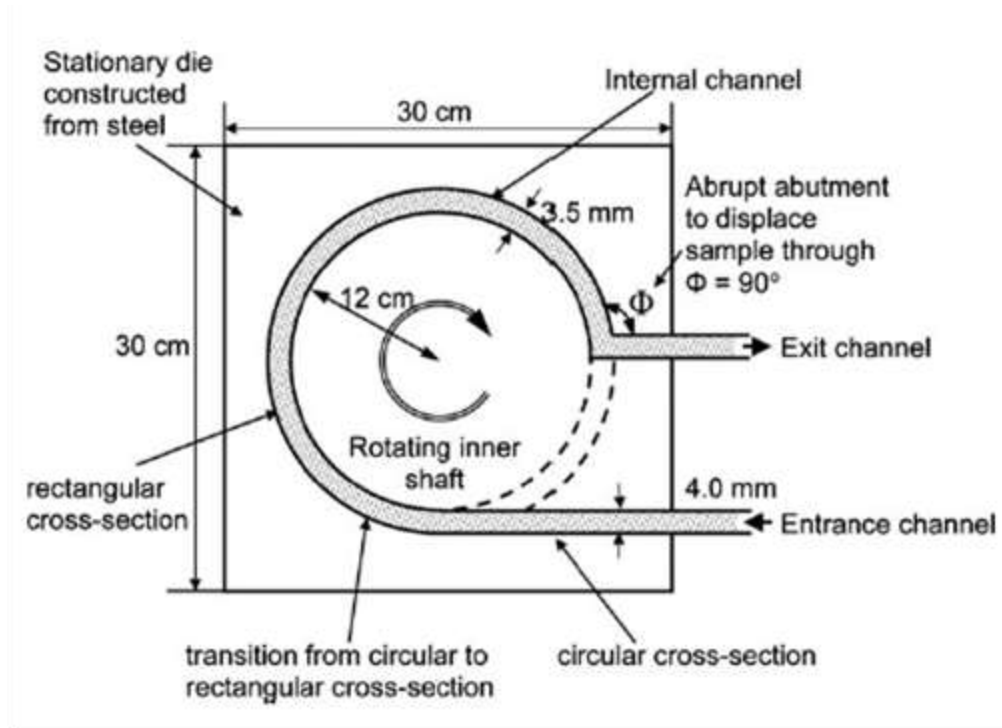
Figure 3. Schematic illustration of the principle of the ECAP–Conform process. Reprinted with
permission from reference [72].

246

D. Producing Gradient Structures and Multi-layered Laminates through Tube Shearing

Multi-layered laminates may be fabricated by ARB when two dissimilar metal sheets are stacked and then subjected to conventional roll bonding. But this procedure requires many cleanings of the metal surfaces and multiple passes through ARB processing so that it is labor-intensive. An alternative approach is to use the process of tube high-pressure shearing (t-HPS) [76]. This latter procedure is based in part on the very early work of Bridgman [77] where tube twisting was introduced as a method of avoiding the problems associated with a lack of strain at the centers of the solid disks. However, the very early work was different because it was based on using a tube sample and then twisting the top with respect to the bottom whereas in t-HPS the sample is again in the form of a tube but the outer surface is sheared around the inner surface by

13

257   placing the tube around a central mandrel, using pressure rings to hold the tube in place and

258   produce high hydrostatic pressures in the tube walls, and then using an outer cylinder to rotate

259   the outer surface with respect to the inner surface.

260   Several experiments have been conducted using t-HPS and the results are encouraging [78].

261   It was shown that, by using two different metals of an AB-type or with four initial interfaces of

262   an ABAB-type, it can be predicted theoretically that there should be a gradient distribution of

263   interfaces with denser stacking at the inner surface of the tube. This is consistent with

264   experiments and there are numerous other predictions based on different sets of initial interfaces

265   [78]. An important result from this work is that t-HPS can be used with an ABAB-type

266   bimetallic tube to produce a multilayered structure. An example is shown in Fig. 4 where the

267   two materials are 5N and 4N Al which were cut to give four interfaces with an ABAB-type

268   initial structure and then the tube was processed by 2 turns to give a very fine grain size (<1 µm)

269   in the 4N Al and a much coarser grain size (~10 µm) in the 5N Al due to the easier grain growth.

270   It is clear from Fig. 4 that the microstructures of each separate component are very well defined

271   and accordingly the results show that this is an excellent procedure for producing a gradient

272   structure [78]. Furthermore, this result is important because of the current considerable interest

273   both in developing and using gradient structures [79-81] and in the fabrication of nano-laminated

274   structures [82].

275
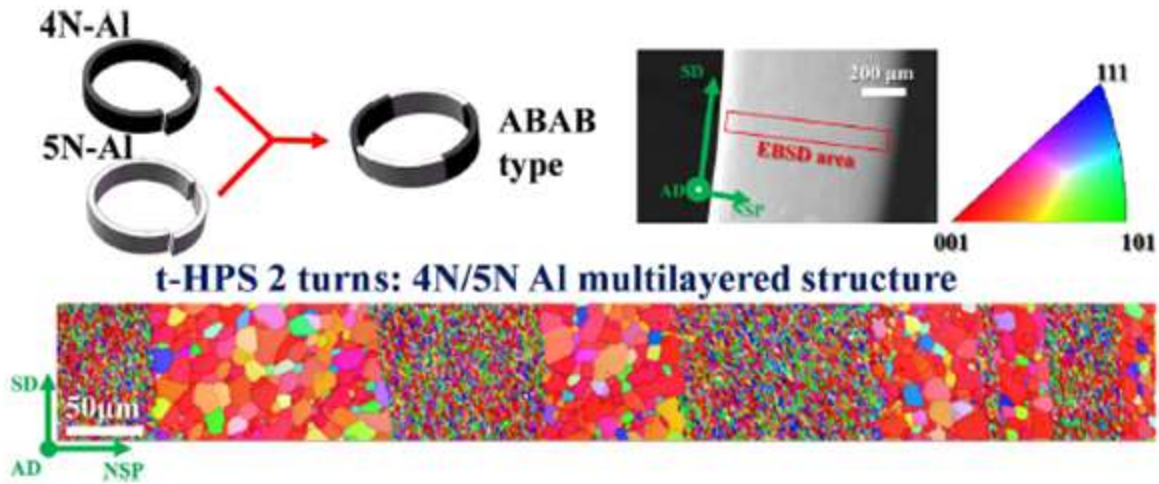
Figure 4. Multilayered structure with alternate distribution of finer and coarser grains fabricated by an ABAB-type 5N-Al/4N-Al bimetallic tube with 2 turns of t-HPS at RT: the 4NAl layers have finer grain size (<1 μm) and the 5N Al layers have relatively coarser grains. Reprinted with permission from reference [78].

E. Using HPT to Process Metal Matrix Nanocomposites

Processing by HPT is generally used to achieve grain refinement in bulk solids. However, the same process has been used also to consolidate metallic powders [83-97], composites [98-102], amorphous compounds [103-107], machining chips [108-110] and ceramic powders [111]. Very recently, new approaches have been developed based on using HPT to bond dissimilar metals and produce solid bulk metallic samples.

The use of dissimilar metals is well established in processing by ARB where sheets of different materials may be conveniently stacked and then processed to form multi-layered microstructures [112-116]. But experiments show that processing by ARB leads to anisotropic plastic behavior, including in strength and ductility, because the properties depend critically upon the precise testing direction cut from the finished product [117]. This suggests it may be

15

293   advantageous to make use of the very high pressures inherent in HPT processing in order to

294   achieve a solid-state reaction.

295   The first attempt to bond dissimilar metals using HPT was in experiments where semi-

296   circular half-disks of Al and Cu were successfully bonded by HPT at RT using a total of up to

297   100 revolutions [118]. Similar experiments were also conducted using four quarter-disks, two

298   each of pure Cu and an Al-6061 alloy, which were positioned to make a complete disk and then

299   processed by HPT for 1 turn at RT to fabricate an Al-Cu hybrid material [119]. This early work

300   confirmed the feasibility of this approach and accordingly extensive experiments were conducted

301   using a commercial purity aluminum Al-1050 alloy and a commercial ZK60 magnesium alloy

302   with the objective of using these materials to synthesize an Al-Mg multi-layered bulk

303   nanostructured material [120-123]. All processing in these experiments was conducted using

304   HPT at RT under quasi-constrained conditions [124,125] with three separate disks placed in the

305   HPT facility in the stacking order of Al/Mg/Al with the Mg disk held between the two Al disks

306   but without using any glue or metal brushing treatment. All stacks of disks were processed

307   under an applied pressure of 6.0 GPa with various numbers of turns up to a total of 10

308   revolutions using a constant rotation rate of 1 rpm.

309   Figure 5 shows three color-coded contour maps that display, using different colors, the

310   values of the measured Vickers microhardness recorded on vertical cross-sectional planes of the

311   disks after processing through 1, 5 and 10 turns, respectively [120]. After 1 turn the hardness is

312   of the order of ~60-70 Hv but after 5 turns the hardness has increased at the edges of the disk and

313   this hardness at the periphery increases even more after 10 turns. Thus, the hardness increases to

314   Hv $\approx$ 130 at the edge after 5 turns but it further increases to Hv $\approx$ 270, equivalent to a tensile

315   strength of ~865 MPa, after 10 turns. These hardness values are exceptionally high and they

16

316   may be compared with values of $Hv \approx 63\text{-}65$ [126] and $Hv \approx 105\text{-}110$ [127] for the Al-1050 alloy

317   and the ZK60 alloy, respectively, after processing by HPT through 5 turns.   Detailed

318   examination by transmission electron microscopy and energy-dispersive X-ray spectroscopy

319   revealed that this high hardness is due to the formation of intermetallic nano-layers of $\beta\text{-Al}_3\text{Mg}_2$

320   and the development after 10 turns of a nanostructured intermetallic compound of $\gamma\text{-Al}_{12}\text{Mg}_{17}$ in

321   the Al matrix in a supersaturated solid solution state.   The extraordinary strength achieved in

322   these experiments through HPT processing of disks of dissimilar metals suggests there is a

323   potential for using this approach to fabricate a wide range of metal matrix nanocomposites

324   (MMNCs).

325
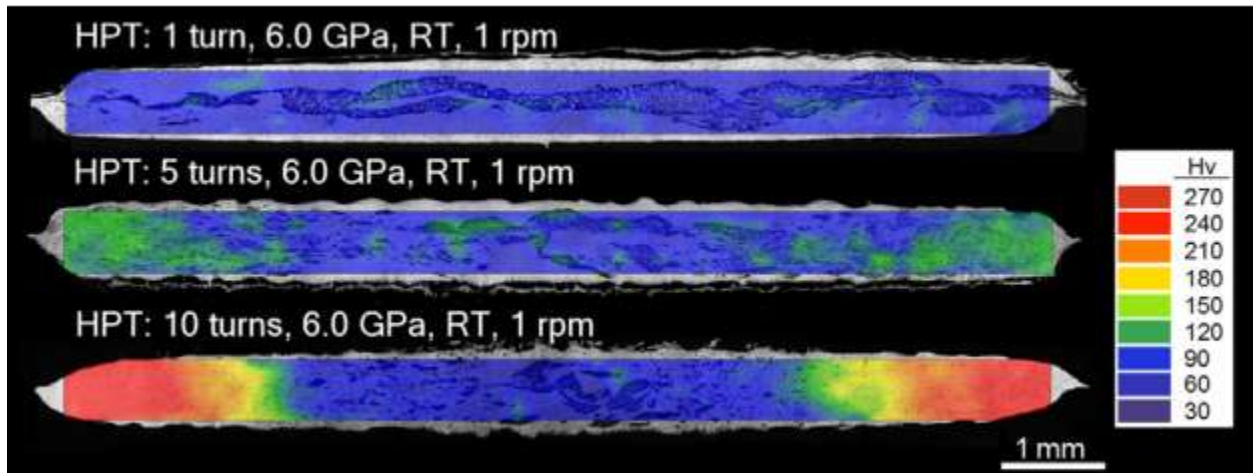
326

327   Figure 5. Color-coded contour maps of the Vickers microhardness for the Al/Mg system after
328   HPT for 1 turn (upper), 5 turns (center) and 10 turns (lower): the values associated with the
329   various colors are given in the hardness color key on the right. Reprinted with permission from
330   reference [120].

331

332   Using the tensile strength of ~865 MPa at the edges of the disk in Fig. 5, the measured

333   strength at the outer edge after 10 turns gives a remarkable strength/weight ratio of ~350 MPa

334   $\text{cm}^3 \text{ g}^{-1}$ and this specific strength is much higher than in many steels or Ti alloys and it is even

17

335 comparable to some strong polymeric engineering composites [128]. Therefore, using the

336 diagram proposed earlier for a very wide range of materials as shown in Fig. 6 [128], it is now

337 appropriate to include the experimentally-synthesized Al-Mg system shown in Fig. 5 where this

338 is denoted in the diagram as HPT-induced aluminum MMNCs without delineating any upper

339 limits to the fracture toughness or the strength-to-weight ratio [122]. It is important to note, from

340 inspection of Fig. 6, that the new MMNC is far superior to conventional Al and Mg alloys

341 (shown by the regions in yellow and red, respectively). Although detailed experiments will be

342 required in the future to precisely define the limits of this approach, it is clear from these early

343 observations that HPT processing of dissimilar metals has a considerable potential for fabricating

344 MMNCs having unusually high strength.

345
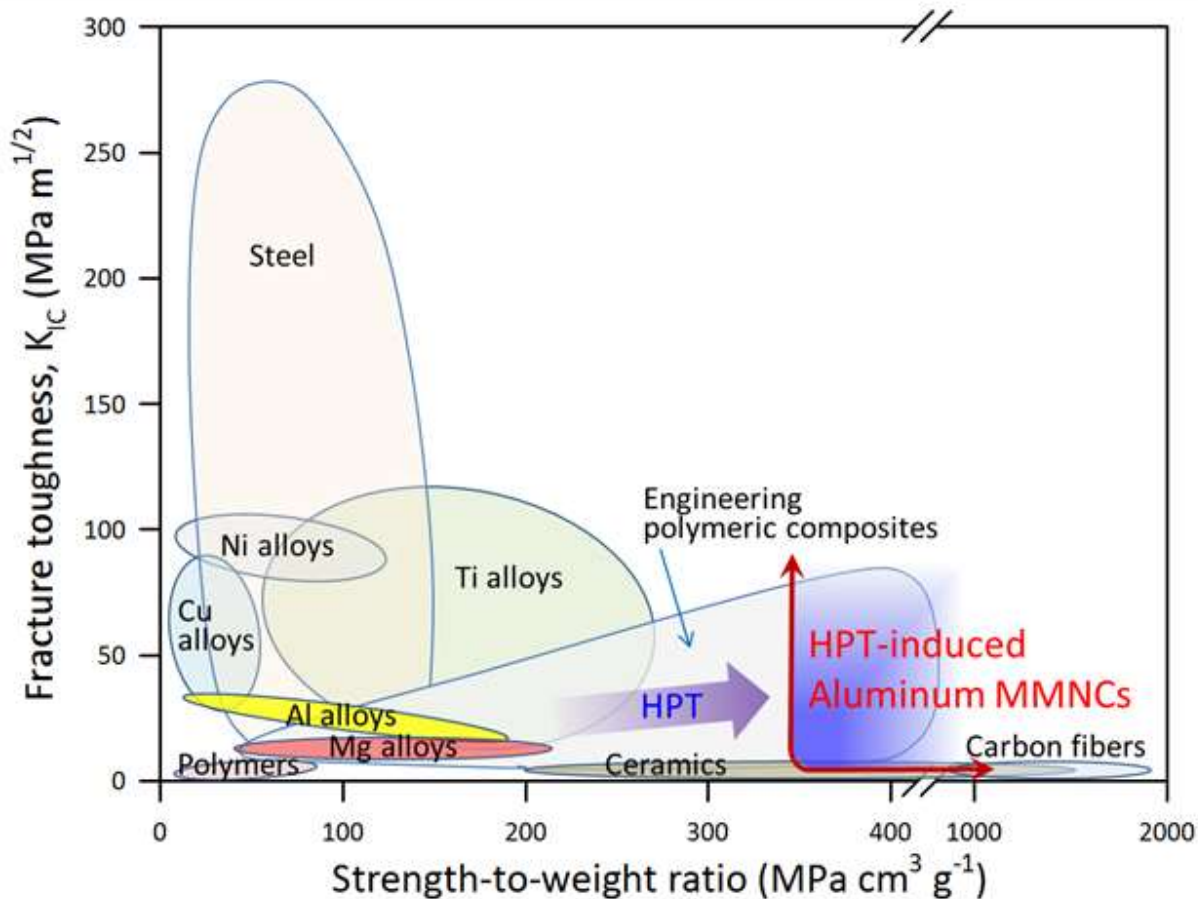
Figure 6. The range of fracture toughness and strength-to-weight ratio for many metals and materials [128] where the synthesized Al-Mg system shown in Fig. 5 after HPT is incorporated into the diagram as HPT-induced aluminum MMNCs without delineating any upper limits for these values. Reprinted with permission from reference [122].

III. BULK NANOSTRUCTURED MATERIALS FROM POWDER PRECURSORS –THE NEED FOR GRAIN SIZE STABILIZATION.

Because grain boundaries are non-equilibrium defects and increase the free energy of a material, the large area of grain boundaries in nanostructured materials provides a large driving force for grain growth. The nanocrystalline grain size is inherently unstable. Significant grain growth, that is, doubling of the initial nanocrystalline grain size in 24 hours, has been observed at room temperature in a number of pure, relatively low melting temperature elements such as Sn,

359   Pb, Al, and Mg [129].   Günther et al. [130] studied grain growth in pure Cu, Ag, and Pd and

360   found grain growth occurring at much lower temperatures than those observed for

361   recrystallization of the elements after heavy cold deformation. In fact, grain growth in Cu and

362   Pd was observed even at room temperature. This is particularly dramatic for Pd which has a high

363   melting temperature of 1825K (1552°C) such that room temperature is only 0.16 of the melting

364   temperature – a very low homologous temperature. Subsequently, Ames et al. [131] observed

365   the grain growth of 10 nm grain size Pd to 10 micron grain size after one month at room

366   temperature. In this case, as in the others of grain growth at room temperature, the initial growth

367   is abnormal. However, at longer times the grain growth changes to normal grain growth.

368   A general expression for grain growth in terms of the velocity of the boundary can be given

369   as: $V = MP$ where M is the grain boundary mobility $= M_o \, exp(-Q_m/RT)$, and $P =$ the driving

370   pressure $= C\gamma/r$, where γ is the specific grain boundary energy, and r is the average grain

371   radius.[132,133]. The two approaches for achieving stabilization of nanoscale grain sizes are

372   then to 1, reduce the mobility, M, by various pinning mechanisms, or 2. To reduce the driving

373   force for grain growth by reducing the specific grain boundary energy, γ.

374   *A. Kinetic stabilization theories and examples of experimental evidence*

375   There are a number of possible mechanisms that have been proposed that may limit the

376   mobility of nanocrystalline grain boundaries. These include porosity drag, solute drag, second

377   phase (Zener) drag, chemical ordering, and grain size stabilization. The most general

378   applicability to a variety of systems and the most important of these mechanisms are solute drag

379   and second phase (Zener) drag.

380   First we discuss the solute drag mechanism. The Cahn [134] Lucke-Stuwe [135] models

381   provide good semi-quantitative account of the effects of solute on grain boundary mobility.

382   According to these models, at low velocities the velocity is inversely proportional to solute

383   concentration. At higher driving forces or lower solute concentrations, there is a transition to a

384   velocity regime where the velocity is independent of solute content. The effect of solute is less

385   at higher temperatures. The solute atmosphere becomes much weaker. Solute drag has been

386   used to explain experimental results of stabilization of a number of nanocrystalline materials, for

387   example Ni-1 at.% Si [136] and Pd – 19 at.% Zr [137].

388   In the second phase (Zener) drag mechanism, the second phase may be a precipitate or

389   dispersoid (e.g. oxide). This pinning effect is less sensitive to temperature than solute drag,

390   especially if a dispersoid is resistant to coarsening. Particle size and distribution play a key role

391   in the effect. The expression for the pinning pressure exerted on the grain boundary by small

392   particles is, in the original Zener formulation [132]

393   *P = 3 fγ/2 r*, where f is the volume fraction of particles randomly distributed of spherical

394   radius r, and γ is the specific grain boundary energy. A refinement of this model [138] gives $D =$

395   0.17*d/f* for low volume fractions, where D is the critical grain size, d the particle size, and f the

396   volume fraction. A large number of experiments on stabilization of nanocrystalline grain sizes

397   have been explained using Zener drag, for example Fe – 10 Al with dispersoids [139].

398   Other mechanisms for decreasing grain boundary mobility include porosity drag, chemical

399   ordering, and grain size effect. Porosity can reduce grain boundary mobility as demonstrated in

400   the grain growth of ceramic TiO_2 prepared by the inert gas condensation method [140]. Reduced

401   grain growth has been observed for ordered nanocrystalline intermetallic compounds, for

402   example Fe_3Si [141]. Grain size stabilization has been predicted by theoretical models and

403   observed experimentally [142]. It is suggested that the decrease in free volume which occurs on

404   grain growth is offset by the non-equilibrium vacancy concentration increases in the matrix as

405   the excess free volume is released on grain growth.

406   *B. Thermodynamic stabilization theories*

407   The general concept of thermodynamic stabilization involves the segregation of solute atoms

408   to the grain boundaries such that the grain boundary energy may be reduced. The reduction of

409   excess interface Gibbs free energy, G, with increasing solute content can be described by the

410   Gibbs adsorption isotherm: $d\gamma = -\Gamma d\mu$ where μ is the chemical potential of the solute atom

411   dissolved in a matrix of solvent atoms, and Γ is the excess amount of solute atoms segregated to

412   the boundary. Plots of $\gamma = dG/dA$ vs. global solute content show a reduction of γ with

413   increasing solute content [143]. Large solute atoms intensify this and could reduce the excess

414   grain boundary free energy with possible grain boundary stabilization at $\gamma = 0$. This γ is not to

415   be confused with grain boundary cohesive energy. Weissmuller [144] was the first to apply

416   these ideas to stabilization of nanocrystalline grain size. His model was based on a dilute

417   solution limit. The equation has the following form: $\gamma = \gamma_o - \Gamma_{sat}[\Delta H_{seg} + RTln(x_c)]$ where γ_o

418   is the grain boundary energy of the pure metal, Γ_{sat} is the solute excess for fully saturated grain

419   boundary interface, ΔH_{seg} is the segregation enthalpy, and $RTln(x_c)$ represents the ideal mixing

420   entropy for bulk solute concentration x_c. This equation implies that the grain size at stabilization

421   decreases as the solute content increases at a fixed temperature. The analysis of Weissmuller

422   was extended by Kirchheim [145] to include the temperature dependence of grain size for a

423   metastable equilibrium state.   The regular solution model of Trelewicz and Schuh [146]

424   eliminates many of the approximations in the previous models, for example, fully saturated grain

425   boundaries or dilute solution approximations. This model has grain boundary regions and bulk

426   regions with variable volume fractions and solute concentrations separated by transitional bonds.

427   ΔG_{mix} is obtained from the difference in the nearest neighbor bond energy and mixing entropy of

428   this system relative to equivalent volumes of unmixed pure A and pure B with no grain

429   boundary. The equilibrium state is obtained by simultaneous minimization of ΔG_{mix} with respect

430   to variations of the solute concentration and the grain boundary volume fraction, subject to

431   conservation of solute. Elastic size misfit enthalpy was not included in this model. A

432   modification of the above model was presented by Saber et al. [147]. A regular solution model

433   for thermodynamic stabilization was based on the Wynblatt-Ku approximation [148] to

434   incorporate both chemical and elastic enthalpy. The equilibrium condition is defined by

435   minimization of the total Gibbs mixing free energy with respect to simultaneous variations in the

436   solute contents and volume fractions with the constraint of overall mass balance. The Lagrange

437   multiplier technique was used to obtain an explicit solution to the constrained equations in a

438   form easily solved using standard numerical software packages. Results for Fe-Zr alloys are

439   given in Figure 7 [147].

440
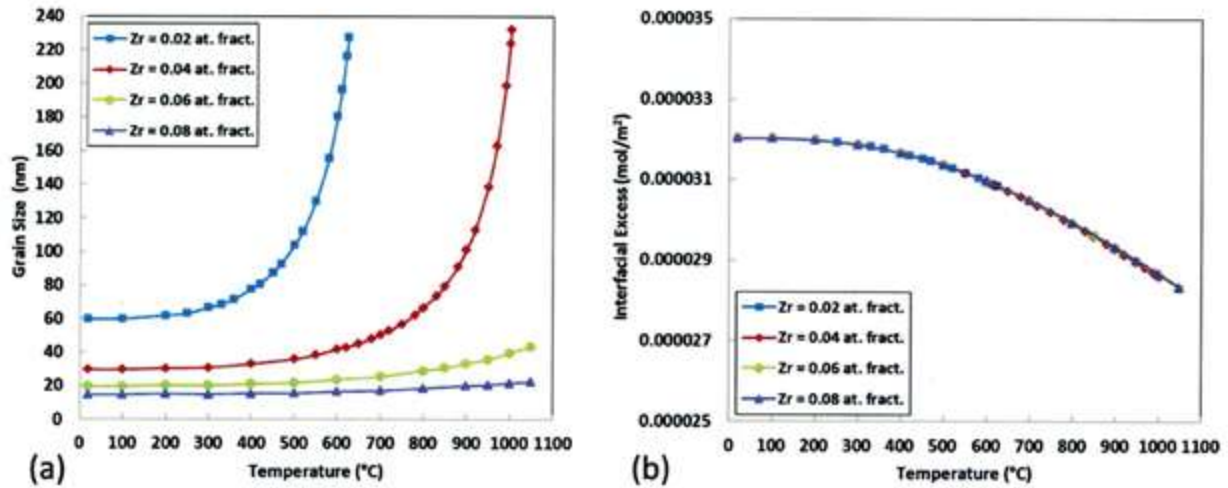
Figure 7. Model predictions of (a) grain size, and (b) interfacial solute excess for Fe-Zr alloys. Reprinted with permission from reference [147].

The previous models did not consider the competition with precipitation of second phases or phase separation. Chookajorn et al. [149] addressed this problem using an analytical approach based on the Trelewicz and Schuh [146] model. They simplified the problem by considering only alloys with positive enthalpies of mixing. Stability maps of enthalpy of segregation vs. enthalpy of mixing were constructed for several elements. One for tungsten is shown in Figure 8.

Subsequently, Schuh and co-workers have extended the range of alloys and details of the grain boundary structure by using Monte Carlo simulations to construct stability maps with six different regions of nanocrystalline stability including duplex nanostructures [150].
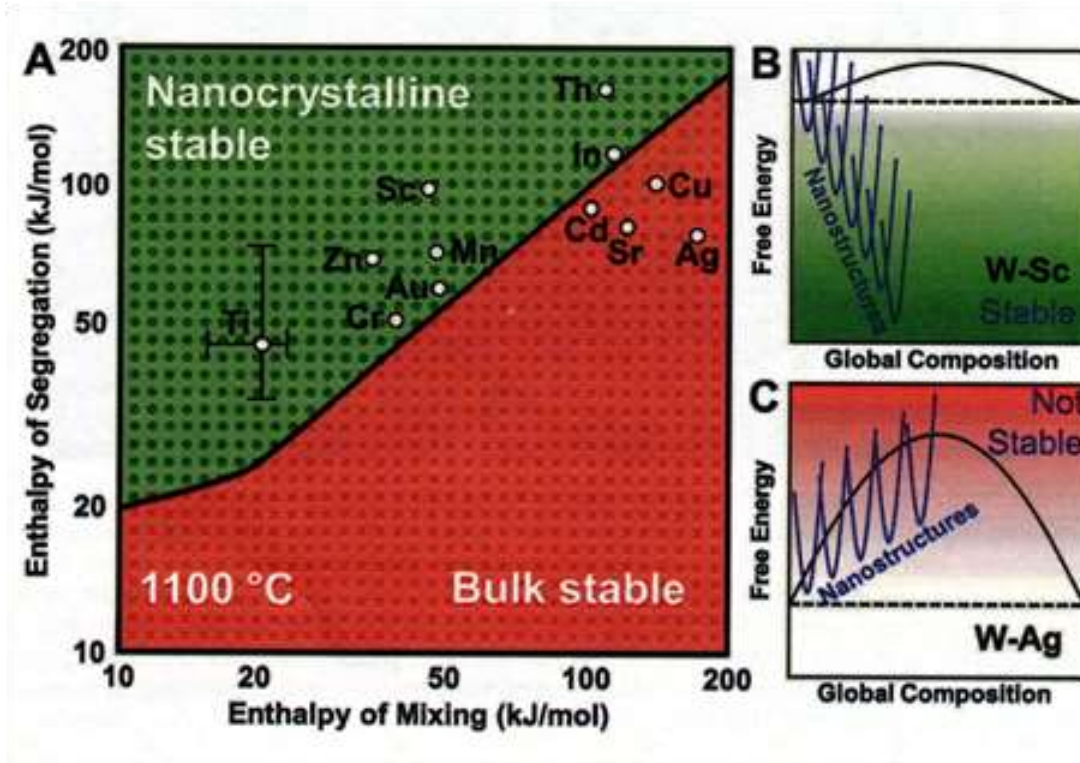
Figure 8. The nanostructure stability map for tungsten-based alloys at 1100oC, calculated on the basis of variation of the enthalpy parameters. For each combination of parameters, the free energy of nanocrystalline structures is compared to that of the bulk regular solution. An example for the nanocrystalline stable region in given in (B) for W-Sc. A bulk stable case is given in (C) for W-Ag. Reprinted with permission from reference [149].

C. Complexions as possible sources of nanocrystalline grain size stabilization

Interface "complexions" are grain boundary "phases" in thermodynamic equilibrium that have stable, finite thicknesses. They were first, and mostly, observed and studied in ceramic materials. Dillon et al. [151] have created a categorization scheme for complexions based on studies of Al_2O_3 doped with calcia, silica, magnesio, or neodymia. The six categories of complexions were identified using high resolution TEM images of the grain boundaries. Rupert [152] has recently reviewed the role of complexions in metallic nanocrystalline materials with regard to thermal stability and deformation. Khalajhedayati and Rupert [153] had reported remarkable thermal stability in nanocrystalline Cu – 3at.% Zr with a nanoscale (54 nm) grain

469   size remaining after heating for a week at 1223K (950°C) (98% of the solidus temperature!).

470   They attributed this stability to segregation at the grain boundary forming amorphous

471   intergranular films (complexions) and to Zener pinning by ZrC nano-particles.

472   *D. Experimental evidence for thermal stability of nanocrystalline alloys*

473   A few examples were given in the section on kinetic stabilization theories of experiments that

474   appear to support this mechanism. In this section, two examples of systems will be given where

475   there is possible contributions to thermal stabilization from both the thermodynamic and kinetic

476   mechanisms. Finally, a comparison will be made using the available data from the literature of

477   thermodynamic, kinetic, combinations of the two, and complexions for stabilization of

478   nanocrystalline alloys as a function of homologous temperature.

479   Example 1. Thermal stability of nanocrystalline Fe-Cr alloys with Zr additions. The

480   influence of 1 to 4 at.% Zr additions to Fe – 10 and 18 at.% Cr alloys on the thermal stability of

481   the nanocrystalline microstructure was studied [154]. Grain sizes were determined by XRD,

482   channeling contrast FIB imaging, and TEM for isochronal annealing treatments up to 1273K

483   (1000°C). Grain size stabilization in the nanoscale range was maintained up to 1173K (900°C)

484   by adding 2 at.% Zr. This is illustrated in Figure 9 where a histogram of the bright field TEM

485   grain size data is given for the Fe – 10 at.% Cr – 2 at.% Zr sample annealed at 1173K. The

486   average grain size for this condition was determined to be 82 nm. Analysis based on the Hall-

487   Petch strengthening and Orowan strengthening was used to extract the volume fraction of

488   intermetallic particles having a mean size of 20 nm. Comparing the TEM grain size with the

489   calculated grain size from the Orowan hardening and Zener pinning models of 168 nm suggests

490   that thermodynamic stabilization may be contributing to the stabilization observed along with

491   Zener pinning.

492   There was no significant difference in the results for the 10 and 18 at.% Cr alloys, which

493   indicates that the bcc to fcc phase transformation does not influence the grain size stabilization in

494   these alloys.

495
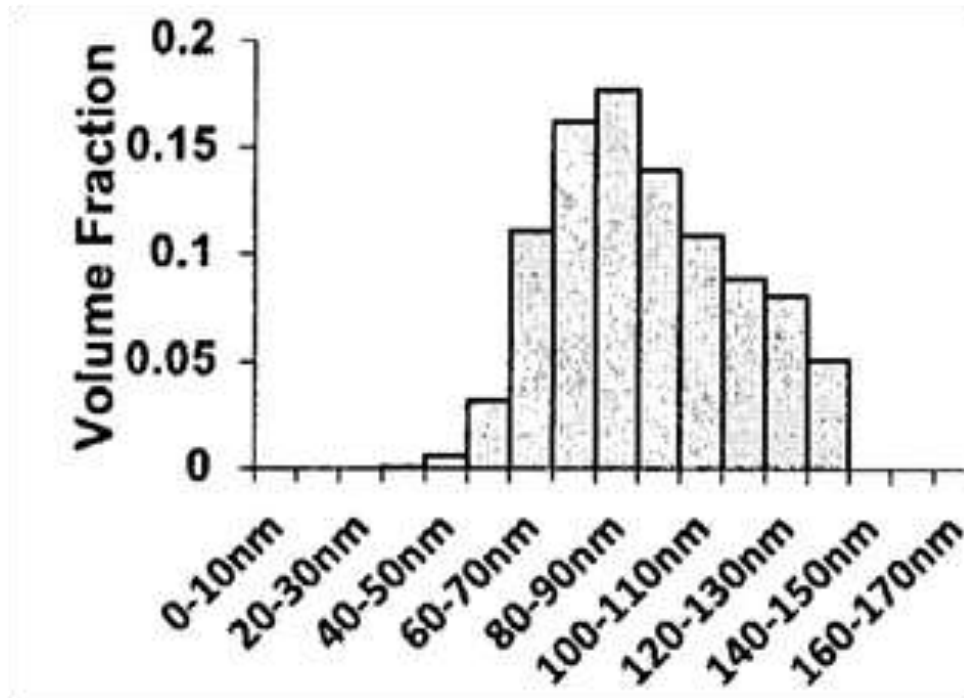
496
497   Figure 9. Bright field grain size histogram for Fe – 10 at.% Cr – 2 at.% Zr sample annealed at
498   1173K (900˚C). Reprinted with permission from reference [154].
499

500   Example 2: High temperature grain size stabilization of nanocrystalline Fe-Cr alloys with Hf

501   additions. Similar to example 1, the influence of 1 to 4 at.% Hf additions on the thermal stability

502   of nanocrystalline Fe – 14 Cr was studied [155].   Hf was selected as a solute addition because

503   the enthalpy of formation of HfO_2 is more negative than that of ZrO_2 indicating that the second

504   phase formation leading to Zener pinning effect might be enhanced compared to the Zr solute

505   additions in Example 1. In addition, the prediction of thermodynamic stabilization for ternary

506   alloys [156] suggests that Hf should be an effective solute for thermodynamic stabilization in Fe

507   -14Cr. Again, XRD, high resolution TEM, channeling contrast FIB imaging, and microhardness

27

508   were obtained for isochronal annealing temperatures up to 1373K(1100°C). It was found that the

509   Fe – 14Cr – 4 at.% Hf alloy exhibited effective grain size stabilization in the nano-scale range up

510   to 1273K (1000°C). The hardness of nearly 5.2 GPa is maintained after annealing at 1273K.

511   The Hall-Petch plot for this alloy along with the base Fe – 14Cr alloy is presented in Figure 10.

512   Employing the Hall-Petch grain size strengthening and Orowan particle strengthening

513   equations for Fe – 14Cr – 4 at.% Hf annealed at 900°C, the deviation of grain size predictions

514   from the actual grain size suggests , as in Example 1, the possibility of a thermodynamic

515   stabilization mechanism contribution due to solute segregation to grain boundaries. The use of a

516   thermodynamic model [156] (prediction given in Figure 11) shows that thermodynamic

517   stabilization can be a viable additional mechanism in conjunction with Zener pinning for

518   stabilizing the nano-grains in Fe - 4Cr – 4 at.%Hf at 1173K (900°C).
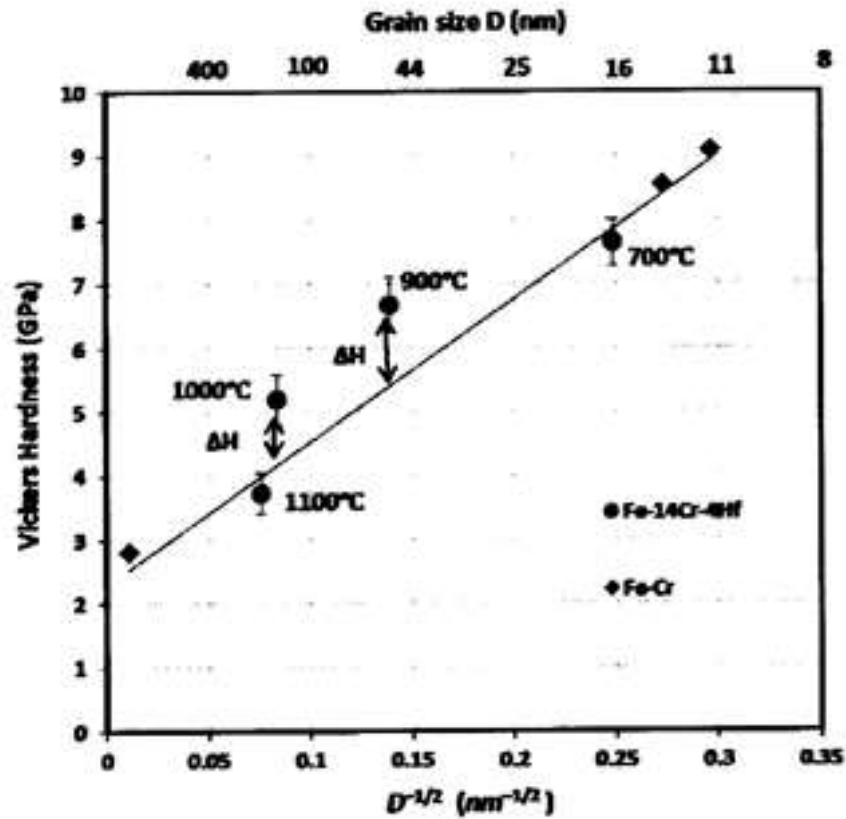
519

520
521   Figure 10. Hall-Petch plot of Fe – 14Cr – 4Hf alloy along with the base Fe – 14Cr alloy.
522   Reprinted with permission from reference [155].
523
524

525
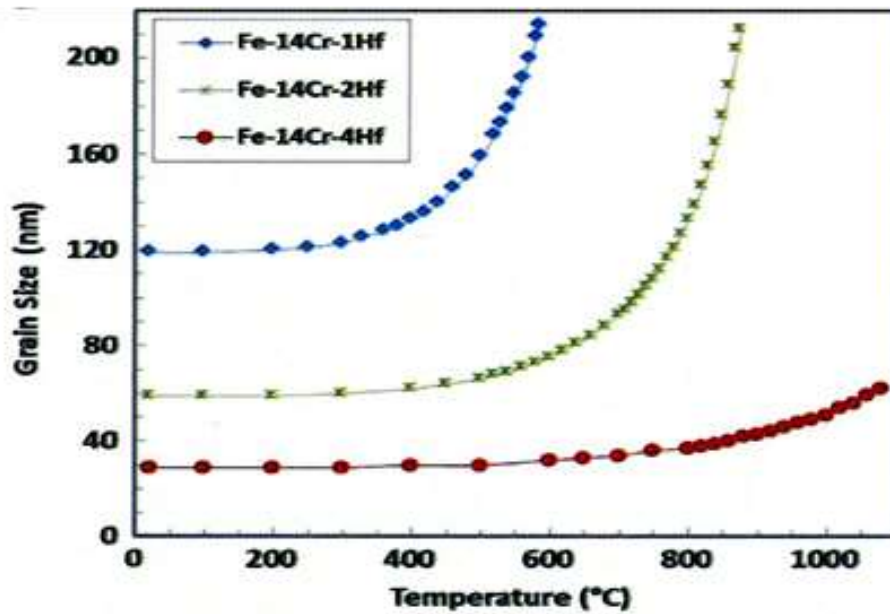
Figure 11. Model prediction for Fe – 14Cr – x Hf alloys for grain size. Reprinted with permission from reference [155].

To summarize this section on the thermal stabilization of nanocrystalline materials we examine data from the literature and looking at the maximum homologous temperature for which the alloy remains nanocrystalline (grain size < 100 nm) and the specifics of the experimental results decide whether the stabilization was due to the thermodynamic mechanism, a kinetic mechanism, a combination of the two, or due to kinetic and complexion stabilization.

From the experimental data shown in Figure 12, it would suggest that the most effective mechanisms for thermal stabilization of nanocrystalline grain size are kinetic (Zener pinning by nanoscale particles) or a combination of this and thermodynamic stabilization by solute segregation to grain boundaries. The one data point for Cu – 3 at.% Zr where Zener pinning is combined with the complexion (an amorphous grain boundary layer) that gives thermal stabilization almost to the melting temperature, points to a possible fertile research field to improve the properties of nanocrystalline alloys.
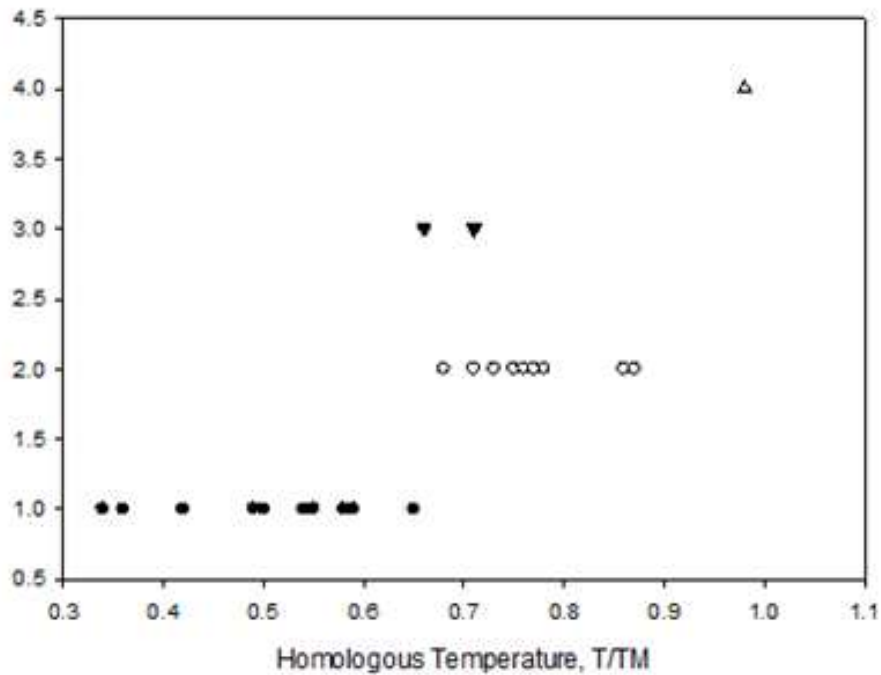
Figure 12. Literature data for thermal stabilization mechanisms vs. maximum homologous temperature for stabilization. The symbols are: thermodynamic stabilization: ●, kinetic stabilization: ○, kinetic and thermodynamic stabilization: ▼, kinetic and complexion stabilization: Δ

IV. CRYOMILLING AND APPLICATIONS

Cryomilling, i.e., mechanical milling of alloys at cryogenic temperatures is representative of a class of powder synthesis techniques that attain the nanostructured state via severe plastic deformation. The cryogenic milling process has attracted considerable interest, primarily as a result of its ability to generate nanocrystalline (NC) and non-equilibrium structures in relatively short time and large quantities. Cryomilled NC powder that can be used to manufacture bulk nanostructured and ultrafine-grained (UFG) alloys with attractive combinations of physical and mechanical properties. Inspection of the scientific literature shows that this technique has been widely used to synthesize NC metals, alloys, and composites, such as Al [157-159]   , Ni [160]

557 Fe [161], Ti [162], Zn [163], Mg [164,165], Pd-10Rh [166], high entropy alloys (HEAs)

558 [167,168], and Al-B$_4$C/SiC composites [169,170]. In certain fcc materials, cryomilling can

559 promote deformation twinning, which is beneficial, given that deformation twins provide for

560 strength enhancement without a loss in ductility. Cryomilling in a liquid nitrogen environment

561 facilitates the formation of nitrogen-containing dispersoids that substantially increase the thermal

562 stability of nanostructures. Thermal stability is critical to retaining fine grain sizes during

563 consolidation of the cryomilled powder when subjected to temperature and pressure. The use of

564 light-weight, higher-strength alloys, such as NC Al alloys, for the construction of vehicles will

565 substantially reduce their weight and lead to improved fuel consumption, range, reliability, and

566 speed. In this section, published data related to cryomilled alloys are reviewed with particular

567 emphasis on cryomilling mechanisms, microstructure, deformation twining, thermal stability of

568 cryomilled powders, and some examples of practical Al alloys fabricated by cryomilling and

569 consolidation.

570 *A. Cryomilling*

571 During cryomilling, the as received powder forms a slurry with a milling attritor, comprising

572 of a rotating impeller within a vessel, and accommodating a flow of incoming cryogenic liquid,

573 normally liquid N$_2$ or liquid Ar. In the laboratories at UC Irvine (Irvine, CA), the system with

574 the largest capability can mill up to 5 kg of Al alloy powder at a time, but there is potential to

575 substantially increase the scale of this operation for commercial exploitation.

576 During cryomilling, similar to conventional mechanical milling, the particles of the powder

577 are repeatedly deformed by compressive and shear stresses arising from being trapped between

578 the balls during collisions and localized rolling. Powder evolution during the milling process

579 generally involves five stages [157,158]: 1) initially, particle flattening as a result of shear band

580 nucleation under localized deformation conditions [171], which then spread throughout the entire

581 sample, forming flakes; 2) when two or more particles are trapped between the balls, they are

582 crushed and cold-welded together to form particles of a larger size with a lamellar structure; 3)

583 equiaxed particle formation due to fracture deformed particles; 4) random welding of powder

584 particles; and 5) steady-state deformation, during which a balance between fracture and cold

585 welding is established as particle size and microstructural refinement progresses. Given that

586 severe plastic deformation during milling is a cyclic process, the milling time dominates the

587 overall deformation strain.

588 Cryomilling leads to the formation of a high density of dislocations in the cryomilled powder

589 because milling induces heavy cyclic deformation, and the cryogenic temperature suppresses the

590 annihilation of dislocations. As an example, a high density of dislocations of 1.7×10^{17} m^{-2} was

591 observed in a cryomilled Al–Mg alloy [172,173]. The dense dislocation networks rearrange to

592 form nanoscale subgrains with low-angle grain boundaries (GBs) during further milling, and

593 then re-orient and transform into grains with high-angle GBs. With an increase in milling time,

594 the mean grain size initially decreases rapidly from the micrometer scale, then slowly decrease

595 down to a saturated value, a few tens of nanometers, determined by the material properties [174,

596 175]. When a minimum grain size is reached, additional straining does not further reduce the

597 grain size because of the intrinsic instability of nano-sized grains. Thus, strain-induced grain

598 refinement ceases as a dynamic balance is reached between structure refinement and coarsening

599 of the refined grains.

600 The value of the minimum grain size that is attained during milling is related to the intrinsic

601 properties of the materials [174] as well as the milling conditions. It has been proposed that the

602 minimum grain size obtainable by milling scales inversely with melting temperature and bulk

33

603   modulus of a material. To that effect a dislocation model was developed to quantitatively

604   describe the minimum grain size obtainable during milling [175]. According to this model, the

605   minimum grain size is governed by the balance between the hardening rate introduced by

606   dislocation generation, and the recovery rate arising from dislocation annihilation and

607   recombination. The minimum grain size, d_{min}, is given by [175]:

608
$$\frac{d_{\min}}{b} = A_3 \exp\left(\frac{-\beta Q}{4RT}\right)\left(\frac{D_{PO}Gb^2}{v_0 k_B T}\right)^{0.25}\left(\frac{\gamma}{Gb}\right)^{0.5}\left(\frac{G}{\sigma}\right)^{1.25}$$
(2)

609   where b is the magnitude of the Burgers vector, A_3 a dimensionless constant, β constant, Q the

610   self-diffusion activation energy, R the gas constant, T the absolute temperature, D_{PO} the diffusion

611   coefficient, G the shear modulus, v_0 the initial dislocation velocity, k_B Boltzmann's constant, γ the

612   stacking fault energy (SFE) and σ is the applied stress. The model predicts that the minimum

613   grain size scales inversely with hardness, proportionally with the SFE and exponentially with the

614   activation energy for recovery.

615   Grain refinement may also occur via recrystallization when a new grain structure forms by

616   nucleation and growth in cold deformed alloys with sufficient stored energy. It is generally

617   argued that recrystallization is not able to occur during cryomilling because recrystallization is

618   thermally activated and depends on a critical temperature and deformation conditions.

619   Interestingly, however, it has been reported that recrystallization does indeed occur in cryomilled

620   Zn [163] and Mg [176]. High density of lattice defects, including stacking faults [177],

621   dislocation, deformation twins [178], and increased GBs generated due to heavy deformation in

622   cryomilled NC hexagonal close packed (HCP) Mg alloys have been reported. In fact, the high

623   density of accumulated lattice defects, particularly dislocations, results in a high stored energy, E

624    $= Gb^2\rho$, which may trigger dynamic recrystallization (DRX) even at cryogenic temperatures. In

625 addition, a high density of dislocations causes the critical temperature for recrystallization T_c to

626 decrease. Recrystallization of cryomilled Mg powder in liquid Ar may also be thermally

627 activated at room temperature due to the presence of relative elevated temperatures (88 K to 298

628 K) when the cryomilled Mg powder is collected at room temperature. The conditions for

629 nucleation of DRX are described by [179]:

630
$$\frac{\rho^3}{\dot{\varepsilon}} > \frac{2\,\gamma_b}{KMLG^2b^5} \qquad\qquad (3)$$

631 where ρ is the dislocation density, $\dot{\varepsilon}$ is the strain rate. γ_b is the specific boundary energy, M is the

632 grain boundary mobility, L is the mean slip distance of the dislocations, G is shear modulus, b is

633 Burger vector, K is a constant. There is a critical value of $\rho/\dot{\varepsilon}$ to be achieved for the nucleation

634 of DRX. When materials with a low SFE, such as Zn, Mg and their alloys with low SFE are

635 deformed at cryogenic temperature, dislocation recovery is slow and the dislocation density

636 could be increased to the critical value necessary for facilitating DRX.

637 The cryomilling technique possesses several characteristics and advantages that distinguish it

638 from the conventional mechanical milling that is typically performed at ambient temperatures,

639 including: 1) powder agglomeration and welding to the milling media are suppressed, resulting

640 in a more efficient milling outcome; 2) oxidation reactions during milling are reduced under the

641 protection of a liquid nitrogen or argon environment; 3) the milling time required to attain a

642 nanostructure is significantly reduced relative to that required of conventional milling. Figure 13

643 shows a comparison of the average grain size evolution with milling time for Zn powder milled

644 at room temperature and at liquid N_2 temperature [179]. It has been consistently reported that

645 the average grain size of cryomilled Zn is consistently smaller than that of room temperature

646 milled Zn with the same amount of milling time. Cryomilling takes the advantage of the

647 extremely low temperature of the liquid N_2 or Ar medium, which suppresses the recovery and

648 leads to more rapid grain refinement and finer grain structures. In addition, the lower temperature

649 also decreases the ductility of the powder, reducing the amount of welding between the particles.

650 Thus, the amount of process control agent (PCA) required to prevent excessive agglomeration of

651 the particles is reduced, decreasing the amount of interstitial contamination introduced during the

652 milling process.

653
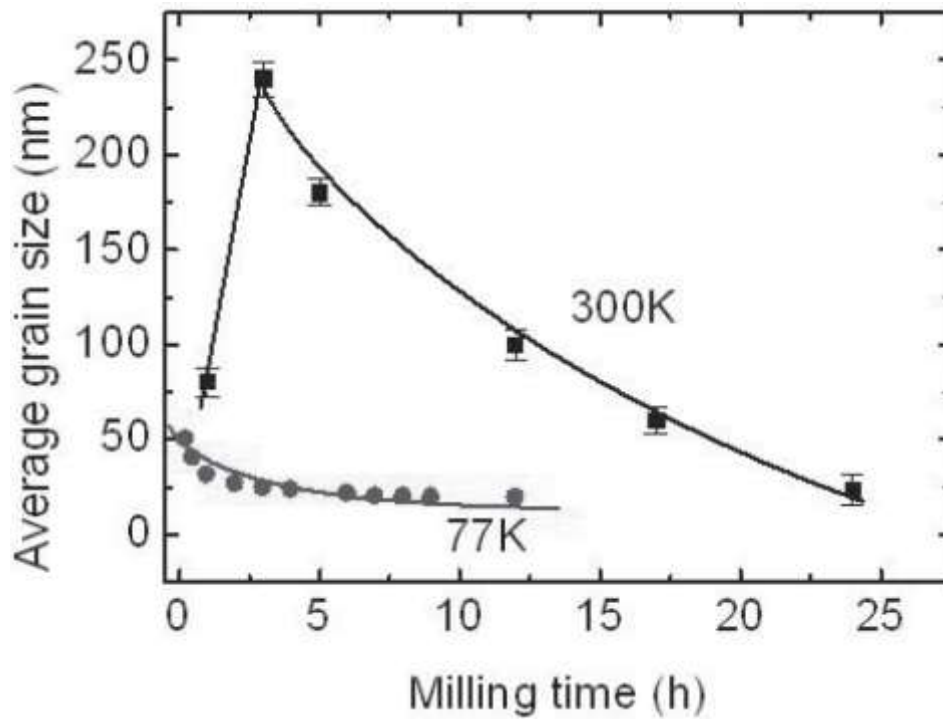
654

655   Figure 13 Comparison of the average grain size evolution with milling time for Zn powder

656 milled at room temperature and at liquid nitrogen temperature. Reprinted with permission from

657 reference [179].

658

659   Even in the presence of hard particles, such as in the case of cryomilling of a

660 matrix/reinforcement (typically a ceramic) mixture, the ductile matrix is deformed, flattened and

661 cold welded [174]. During cryomilling the reinforcement particles are entrapped in the matrix

662   material, which can eliminate the voids between the matrix and the ceramic reinforcement and

663   potentially promote solid state bonding between them. Another advantage of using cryomilling

664   to synthesize metal matrix composite powders is that it facilitates the formation of a

665   homogeneous distribution of the reinforcement particles in the matrix. Conventional blending

666   methods often lead to clustering of the reinforcement, resulting in poor mechanical behavior.

667   Published studies suggest that a homogeneous distributions of reinforcements in a matrix can

668   readily be achieved by using cryomilling 169,170].

669   In addition, the presence of hard particles in a powder mixture can facilitate deformation and

670   fracture of the matrix and thereby facilitate grain refinement. As a consequence, a shorter milling

671   time may be required to attain steady state conditions during milling. In related studies it was

672   reported that the introduction of a small volume fraction of AlN particles (2 μm) into Ni

673   facilitated grain refinement during cryomilling [180]. This enhancement was rationalized on the

674   basis of the interactions of dislocations with hard particles, and the thermally induced dislocation

675   generation due to the difference in thermal expansion coefficient between matrix and

676   reinforcement [180,181].

677   *B. Deformation Twining by Cryomilling*

678   It is well known that NC alloys are significantly stronger than their coarse-grained

679   counterparts [157,182], but their ambient temperature uniform tensile ductility is usually

680   disappointingly low due to the fact that GBs experience much larger plastic strain than that

681   sustained by grain interiors. Attempts to retain or increase the ductility during grain refinement

682   have frequently resulted in reduced strength [182,183]. However, it was reported that dislocation

683   accumulation at twin boundaries in NC metals provides strength enhancement without a loss in

684   ductility [184,185]. Twin boundaries with extremely low excess energy can effectively hinder

685   dislocation motion, acting as stable interfaces leading to the increase of both the strength and

686   ductility in NC materials [186,187]. Moreover, it has been well documented that a smaller grain

687   size impedes deformation twinning and there are many experimental studies providing support to

688   this finding [188-191]. On one hand, the stress required for activating twinning increases much

689   faster with decreasing grain size relative to that required for dislocation slip which competes with

690   twinning; accordingly, a smaller grain size renders deformation twinning more difficult. On the

691   other hand, a lower temperature and higher strain rate usually promote deformation twinning

692   [191]. The increase in twinning tendency at low temperatures and higher strain rates can be

693   largely attributed to the increase in flow stress of materials, which increases with decreasing

694   temperature and increasing strain rate. When flow stress increases, the motion of dislocations

695   becomes more difficult, while deformation twining readily occurs. There is an equivalent effect

696   of low temperature and high strain rate, as the dislocation generation rate is faster than the

697   annihilation of dislocation during deformation at low temperature and high strain rates [191]. As

698   cryomilling is characterized by relatively high strain rates (up to 6.35×10^3 s^{-1} [192]) and

699   cryogenic temperatures, deformation twinning is facilitated in cryomilled metals and alloys.

700   In the face centered cubic (FCC) case, the twinning plane is the close-packed (111), and twin

701   nucleation and growth are controlled by well-defined partial dislocations that co-operatively

702   move and propagate on successive (111) planes [194]. A material with high SFE, such as Al

703   (160- 200 J/m^2), will be less susceptible to twinning than materials with low SFE, like Cu alloys

704   (70-78 J/m^2). SFE is equivalent to twin energy, and the propensity for deformation twinning

705   increases with decreasing SFE [195]. Twins are abundant in many low SFE metals, but are rarely

706   seen in high SFE metals like Al [196-198], because when the SFE is low, the mobility of

707   dislocations in a material decreases, while deformation twining become more feasible. Notably,

708   the first report of twinning in NC fcc Al was observed in cryomilled Al [193], as shown in

709   Figure 14, which shows an HRTEM image of twin with dimension of approximately 10 nm in

710   cryomilled Al-7.5Mg powder. The black arrow shows that atoms on (110) have a strain along

711   <112> direction, and twinning occurred on the (111) plane.
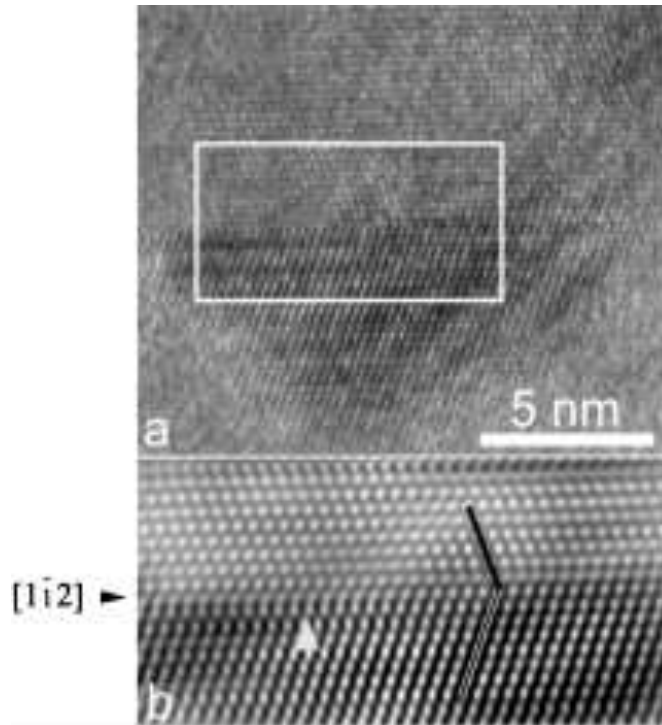
712

713   Figure 14 HREM image of Al-7.5Mg alloy cryomilled for 8 h, (a) Image of a whole

714   nanoscale twin. (b) Local magnification of a twin. Reprinted with permission from reference

715   [193].

716

717   In most HCP metals and alloys, deformation twins are readily nucleated. This is true, for

718   example, in the case of coarse grained Mg and Mg alloys, due to the low SFE of Mg (30 mJ/m^2

719   [199]) in combination with a limited number of independent slip systems. The SFE in Mg-(3-

720   9wt.%) Al alloys is 5.8-27.8 mJ/m^2, and decreases with increasing Al content [200]. For HCP

721   Mg, the activation of primary slip system is limited and hindered on account of large CRSS

722 values at cryogenic temperature. Twinning, however, remains a deformation mechanism that

723 could be activated with secondary slip of partial dislocations under these conditions. The low

724 temperature renders recovery more difficult by limiting the mobility of dislocations [201].

725 Lattice friction stress also strongly depends on temperature, and increases with decreasing

726 temperature [202], which makes dislocation glide through the lattice and GB sliding more

727 difficult. As deformation intensity increases at cryogenic temperatures with high strain rate, the

728 number of dislocations increases, and a higher dislocation density accumulates on the GB

729 regions, which lead to a highly localized stress concentration at GBs, and act as the driving force

730 for twinning nucleation. In essence, the combination of low temperature and high local stresses

731 that is characteristic of cryomilling promote the activation of twinning mechanisms.

732 During cryomilling, the flow stress of Mg increases with decreasing temperature and

733 increasing strain rate [203], and accordingly so does the critical stress required to nucleate and

734 propagate a twin. The most commonly observed twinning plane is the (10-12) in the <10-1-1>

735 direction for Mg [204]. This phenomenon has now been documented in a number of NC Mg

736 alloys, such as Mg-10at.%Ti [205], Mg-30wt.%Al [206], as well as cryomilled AZ80 (Mg-

737 8wt.%Al-0.5wt.%Zn)[164]. Moreover the formation of nano-sized twins in cryomilled pure Mg

738 powders was documented using HRTEM [165]. The formation of nano twins in NC pure Mg was

739 attributed to the combination of: a high strain rate, cryogenic temperature, and high local shear

740 stresses present around the GBs during deformation by cryomilling. Such low temperature

741 deformation processing has also been reported to facilitate deformation twinning in other

742 cryomilled NC alloys and ceramics, such as Al-7%Mg [193, 207-209], Cu [210], and B_4C [211].

743 The formation of twins by cryomilling provides a promising approach to improve the mechanical

744 properties of NC metals and alloys.

C. Thermal Stability of Cryomilled Alloys

746   NC metals and alloys are thermally unstable when compared to the behavior of their coarse-

747   grained counterparts. From a thermodynamic viewpoint, nano-grains grow at lower temperatures

748   than those required by their coarse grained counterparts [212,213]. There is a large amount of

749   enthalpy that is stored in the high-density GBs, which provides a substantial driving force for

750   grain coarsening [186]. The reduced thermal stability of nanostructured materials not only limits

751   their technological and practical applications, but also renders their processing a challege.

752   A review of the literature reveals that there are kinetic and/or thermodynamic strategies that

753   have been proposed in an effort to stabilize metallic nanostructures [213]. One approach involves

754   the pinning of GBs by promoting the drag of second-phase, solutes, and chemical ordering [214]

755   in order to decrease their mobility for kinetic stabilization. From a thermodynamic perspective,

756   the driving force of grain coarsening is proportional to the grain-boundary energy. The specific

757   grain-boundary energy can be reduced by solute segregation in the GBs, resulting in a high

758   entropy GBs[214,215]. A theoretical framework that incorporates the influence of second-phase

759   particles and solute segregation at GBs on stress-induced GB migration and grain rotation was

760   formulated [216]. The modelling results suggest that both second-phase particles and solute

761   atoms segregated at GBs reduce the rate of GB migration and grain rotation.

762   Cryomilling in a liquid N_2 environment generates nitrogen containing nano-sized dispersoids

763   are formed [217-219] which can increase the strength of the alloys by pinning dislocations [161].

764   The significance of the nitrogen-containing dispersoids is that they substantially increase the

765   thermal stability of the microstructure for Al-containing alloys [219-221]. This is important in

766   retaining fine grain sizes during consolidation when the cryomilled powder subjected to

767 temperature and pressure, the combined effects of which would otherwise lead to rapid grain

768 growth.

769   A low ductility and limited thermal stability represent intrinsic limitations of NC structural

770 materials. Stabilizing nanostructures by interface complexions to decrease the grain-boundary

771 mobility does not improve their ductility. It is necessary to provide work-hardening and strain

772 delocalization during deformation in the nanostructures to enhance their ductility [186]. In

773 related work it has been reported that twin boundaries with extremely low excess energy

774 effectively hinder dislocation and GBs motion and can thus act as stable interfaces. Twin

775 boundaries with nanoscale spacing are effective to improve strength, ductility and thermal

776 stability. This might be another reason for the observed high thermal stability of cryomilled

777 nanostructured materials because cryomilling can promote deformation twining [9, 37].

778   There are numerous published studies documenting the thermal stability of cryomilled alloys.

779 For example, in the case of cryomilled 5083 Al alloy processed via HIP and extrusion results

780 from creep tests at two temperatures: 573 and 623 K [222] show surprising thermal stability. An

781 average grain size of 200 nm was observed in the microstructure of the cryomilled 5083 Al.

782 After a long time exposure for nearly 1000 h at temperatures of 573 and 623 K (0.61–$0.66T_m$,

783 where T_m is the melting temperature of the materials), there is only a slight grain growth. An

784 average grain size of approximately 220 nm and an average grain size of approximately 280 nm

785 were observed after holding for 996 h at a temperature of 573 K and 938 h at a temperature of

786 623 K, respectively. After holding at elevated temperatures, fine precipitates of approximately

787 20–50 nm were observed. During cryomilling in liquid N_2, most of the alloying elements are

788 essentially dissolved into the aluminum matrix, forming a supersaturated solid solution. Small

789 amounts of impurity elements (O, N, C, H, Fe, Cr, etc.) are also introduced into the Al alloys

42

790   during cryomilling, with some of them forming nanoscale dispersions [223], which can enhance

791   the retarding force on GB migration. The presence of second phases (nanoscale aluminum

792   oxides, nitrides, carbides, or precipitates), in combination with GB segregation of solute and/or

793   impurity elements is considered to play a significant role in stabilizing the microstructure.

794   Burke developed a model of grain growth based on the drag forces exerted by the dispersion

795   particles on the migrating GBs [224]. In this model, it is considered that the grain growth rate is

796   controlled by the decreasing difference between the ultimate limiting grain size and the changing

797   value of the instantaneous grain size. Burke assumed that the drag force is independent of grain

798   size, which is reasonable under the condition that the source of pinning does not depend on grain

799   size. This situation exists when pinning is produced from dispersion particles or pores. Burke's

800   model may be expressed by the following equation:

801
$$\frac{D_0 - D}{D_m} + \ln\left(\frac{D_m - D_0}{D_m - D}\right) = \frac{k_0 t}{D_m^2} \exp\left(\frac{-Q}{RT}\right)$$
(4)

802   where D is the average instantaneous grain size, k_0 is a constant and Q is the activation energy

803   for grain growth, t is the annealing time, and D_m is the limiting ultimate grain size for the

804   particular annealing temperature. By differentiating Eq. (4), the following growth rate equation is

805   obtained:

806
$$\frac{\mathrm{d}D}{\mathrm{d}t} = k\left(\frac{1}{D} - \frac{1}{D_m}\right)$$
(5)

807   From the linear plot of $dD/dt - 1/D$, the value of slope (k) at the different annealing

808   temperature can be determined. Using Beck's equation, the value of activation energy for grain

809   growth can be determined from the plot of $ln(k)$ as a function of $1000/RT$ [221]. From values of

810   activation energy for grain growth, two-grain growth regimes were identified: the low-

811   temperature region (<573 K (300°C)) and the high-temperature region (>573 K (300°C)). For

812   temperatures lower than 573 K (300°C), the activation energy of 25 ± 5 kJ/mol was determined.

813   This low activation energy represents the energy for the reordering of GBs in the UFG material.

814   For temperatures higher than 573 K (300°C), the activation energy of 124 ± 5 kJ/mol was

815   measured. This activation energy, 124 ± 5 kJ/mol, lies between that for GB diffusion and lattice

816   diffusion in analogous Al polycrystalline systems [221].

817   *D. Engineering Applications*

818   A specific example of a practical application of cryomilled NC Al alloys involves target

819   components in the U.S. Marine Corps Assault Amphibious Vehicle (AAV7A1) [225], which

820   provides a range of services on a battlefield. The weight of an empty AAV7A1 is 21 t, and the Al

821   hull, made from Al 5083 (Al-4.4Mg-0.7Mn-0.15Cr, UTS of 310 MPa), contributes about 14 t to

822   this weight. Another significant proportion of the additional weight is the steel armor that is

823   bolted on. Reducing the overall weight of the AAV7A1 is a prime objective given the need to

824   decrease the fuel consumption. As a consequence, an important technical goal is to increase the

825   strength of the Al 5083 while retaining its welding and anticorrosion properties, and

826   consequently decreasing the overall amount of material required (and thereby overall weight).

827   Similarly, improving the ballistic performance of Al 5083 will also decrease the amount of

828   additional steel armor needed. Initial results obtained from a research program funded by the

829   Navy suggests that these dual objectives can be achieved through the implementation of

830   cryomilling, which can produce NC Al 5083 with a UTS greater than 700 MPa [159]. In terms

831   of ballistics performance, the resistance of consolidated (HIP, extrusion, and rolling) cryomilled

832   Al 5083 strip against a small-caliber, armor-piercing threat has been established and based on the

833   test results [69], it is estimated that, a 13 mm thick cryomilled plate is equivalent to a 19 mm

834　standard plate, which represents 33% less weight required to stop the same threat, saving over

835　4.5 t on a hull weighing 14 t.

836　　　In terms of corrosion, comparison tests of consolidated cryomilled Al 5083 with standard

837　coarse grained Al 5083 were completed to evaluate their corrosion behavior in salt-containing

838　aqueous solutions and their susceptibility to intergranular corrosion in the nitric acid mass loss

839　test [226]. Results show that there was not a significant difference in the corrosion behavior

840　between the two types of materials, and that the cryomilled material exhibited less susceptibility

841　to intergranular corrosion.

842　　　Finally, in terms of joining, tungsten inert gas welding was used to join a plate made from

843　cryomilled materials to a standard Al 5083 plate, resulting in a weld with the same hardness as

844　that of the standard plate. Similarly, two tubes of cryomilled Al 5083 were inertia welded

845　together, without any drop in hardness at the weld interface [225]. The hardness of a joint of

846　friction-stir welded cryomilled Al 5083 dropped slightly to ~125 diamond-pyramid hardness

847　(DPH).

848
849
850　**ACKNOWLEDGEMENTS**
851

858

859   **REFERENCES**

860   1.   H. Gleiter, Progress in Materials Science, (1989) **33**, 223-315.

861   2.   U. Erb, K. T. Aust, G. Palumbo, Chapter 6 in Nanostructured Materials, Processing,
862   Properties, andApplications, 2nd edition, ed. C. C. Koch, William Andrew, Norwich, NY
863   2007.

864   3.   Y. Yoshizawa, S. Oguma, K. J. Yamauchi, J. Appl. Phys.(1988) **64**, 6044.

865   4.   R. Z. Valiev, R. K. Ishamgaliev, I. V. Alexandrov, Prog. Mater. Sci. (2000) **45**, 103.

866   5.   J. R. Groza and R. J. Dowding, NanoStructured Materials, (1996) **7,** 749.

867   6.   S. Yu, C-J. Sun, G-M. Chow, Chapter 1 in Nanostructured Materials, Processing,
868   Properties , and Applications, 2nd edition, ed. C. C. Koch, William Andrew, Norwich, NY,
869   2007.

870   7.   R.Z. Valiev, Y. Estrin, Z. Horita, T.G. Langdon, M.J. Zehetbauer, and Y.T. Zhu: *JOM*,
871   2006, vol. 58 (4), pp. 33-39.

872   8.   J.T. Wang: *Mater. Sci. Forum*, 2006, vol. 503-504, pp. 363-370.

873   9.   T.G. Langdon: *Mater. Sci. Forum*, 2011, vol. 667-669, pp. 9-14.

874   10.   S. Srinivasan and S. Ranganathan: *India's Legendary Wootz Steel: An Advanced Material*
875   *of the Ancient World*, National Institute of Advanced Studies and IISc, Bangalore, India,
876   2004.

877   11.   O.D. Sherby and J. Wadsworth: *J. Mater. Proc. Technol.*, 2001, vol. 117. pp. 347-363.

878   12.   P.W. Bridgman: *Phys. Rev.*, 1935, vol. 48, pp. 825-847.

879   13.   P.W. Bridgman: *Studies in Large Scale Plastic Flow and Fracture*, McGraw-Hill, New
880   York, NY, U.S.A., 1952.

881   14.   K. Edalati and Z. Horita: *Mater. Sci. Eng. A*, 2016, vol. A652, pp. 325-352.

882   15.   N.A. Smirnova, V.I. Levit, V.I. Pilyugin, R.I. Kuznetsov, L.S. Davydova, and V.A.
883   Sazonova: *Fiz. Metal. Metalloved.*, 1986, vol. 61, pp. 1170-1177.

884   16.   V.M. Segal, V.I. Reznikov, A.E. Drobyshevskiy, and V.I. Kopylov: *Russian Metal.*, 1981,
885   vol. 1, pp. 99-105.

886   17.   R.Z. Valiev, O.A. Kaibyshev, R.I. Kuznetsov, R.Sh. Musalimov, and N.K. Tsenev: *Dokl.*
887   *Akad. Nauk SSSR*, 1988, vol. 301, pp. 864-866.

888   18.   T.G. Langdon: *Int. J. Mater. Res*., 2007, vol. 98, pp. 251-254.

889   19.   R.Z. Valiev, N.A. Krasilnikov, and N.K. Tsenev: *Mater. Sci. Eng. A*, 1991, vol. A137, pp.
890   35-40.

891   20.   R.Z. Valiev, A.V. Korznikov, and R.R. Mulyukov: *Mater. Sci. Eng. A*, 1993, vol. A168,
892   pp. 141-148.

893   21.   Y. Saito, N. Tsuji, H. Utsunomiya, T. Sakai, and R.G. Hong: *Scr. Mater.*, 1998, vol. 39, pp.
894   1221-1227.

895   22.   Y. Saito, H. Utsunomiya, N. Tsuji, and T. Sakai: *Acta Mater.*, 1999, vol. 47, pp. 579-583.

896   23.   O.R. Valiakhmetov, R.M. Galeyev, and G.A. Salishchev: *Fiz. Metall. Metalloved,* 1990,
897   vol. 10, pp. 204-206.

898   24.   S.V. Zherebtsov, G.A. Salishchev, R.M. Galeyev, O.R. Valiakhmetov, S.Yu. Mironov and
899   S.L. Semiatin: *Scripta Mater*., 2004, vol. 51, pp. 1147-1151.

900   25.   B. Cherukuri, T.S. Nedkova, and R. Srinivasan: *Mater. Sci. Eng. A*, 2005, vol. A410-411,
901   pp. 394-397.

902 26. A. Kundu, R. Kapoor, R. Tewari, and J.K. Chakravarty: *Scr. Mater.*, 2008, vol. 58, pp.
903   235-238.
904 27. J. Richert and M. Richert: *Aluminium*, 1986, vol. 62, pp. 604-609.
905 28. M. Richert, H.P. Stüwe, M.J. Zehetbauer, J. Richert, R. Pippan, Ch. Motz, and E. Schafler:
906   *Mater. Sci. Eng.A*, 2003, vol. A355, pp. 180-185.
907 29. Y.T. Zhu, H.G. Jiang, J.Y. Huang, and T.C. Lowe: *Metall. Mater. Trans.,* 32A (2001), pp.
908   1559-1562.
909 30. J.Y. Huang, Y.T. Zhu, H.G. Jiang, and T.C. Lowe : *Acta Mater.,* 49 (2001), pp. 1497-1501.
910 31. Y. Beygelzimer, D. Orlov, and V. Varyukhin: *Ultrafine Grained Materials II*, ed. Y.T.
911   Zhu, T.G. Langdon, R.S. Mishra, S.L. Semiatin, M.J. Saran, T.C. Lowe, TMS, Warrendale,
912   PA, pp. 297-304 (2002).
913 32. V. Varyukhin, Y. Beygelzimer, S. Synkov, and D. Orlov: *Mater. Sci. Forum*, 2006, vol.
914   503-504, pp. 335-340.
915 33. T.G. Langdon: *Acta Mater.* 2013, vol. 61, pp. 7035-7059.
916 34. A.P. Zhilyaev, S. Lee, G.V. Nurislamova, R.Z. Valiev, and T.G. Langdon: *Scr. Mater.*,
917   2001, vol. 44, pp. 2753-2758.
918 35. A.P. Zhilyaev, G.V. Nurislamova, B.K. Kim, M.D. Baró. J.A. Szpunar, and T.G. Langdon:
919   *Acta Mater.*, 2003, vol. 51, pp. 753-765.
920 36. J. Wongsa-Ngam, M. Kawasaki, and T.G. Langdon: *J. Mater. Sci.*, 2013, vol. 48, pp. 4653-
921   4660.
922 37. X.C. Xu, Q. Zhang, N. Hu, Y. Huang, and T.G. Langdon: *Mater. Sci. Eng. A*, 2013, vol.
923   A588, pp. 280-287.
924 38. P.M. Bhovi, D.C. Patil, S.A. Kori, K. Venkateswarlu, Y. Huang, and T.G. Langdon: *J.
925   Mater. Res. Tech.*, 2016, vol. 5, pp. 353-359.
926 39. R.Z. Valiev and T.G. Langdon: *Prog. Mater. Sci.*, 2006, vol. 51, pp. 881-981.
927 40. Y. Iwahashi, J. Wang, Z. Horita, M. Nemoto, and T.G. Langdon: *Scr. Mater.*, 1996, vol.
928   35, pp. 143-146.
929 41. M. Furukawa, Z. Horita, Y. Iwahashi, M. Nemoto, and T.G. Langdon: *Mater. Sci. Eng. A*,
930   1998, vol. A257, pp. 328-332.
931 42. Y. Iwahashi, Z. Horita, M. Nemoto, and T.G. Langdon: *Acta Mater.*, 1997, vol. 45, pp.
932   4733-4741.
933 43. Y. Iwahashi, Z. Horita, M. Nemoto, and T.G. Langdon: *Acta Mater.*, 1998, vol. 46, pp.
934   3317-3331.
935 44. M. Kawasaki, Z. Horita, and T.G. Langdon: *Mater. Sci. Eng. A*, 2009, vol. A524, pp. 143-
936   150.
937 45. C. Xu, M. Furukawa, Z. Horita, and T.G. Langdon: *Mater. Sci. Eng. A*, 2005, vol. A398,
938   pp. 66-76.
939 46. M. Prell, C. Xu, and T.G. Langdon: *Mater. Sci. Eng. A*, 2008, vol. A480, pp. 449-455.
940 47. C. Xu, Z. Horita, and T.G. Langdon: *Mater. Sci. Eng. A*, 2011, vol. A528, pp. 6059-6065.
941 48. A.P. Zhilyaev and T.G. Langdon: *Prog. Mater. Sci.*, 2008, vol. 53, pp. 893-979.
942 49. R.Z. Valiev, Yu.V. Ivanisenko, E.F. Rauch, and B. Baudelet: *Acta Mater.*, 1996, vol. 44,
943   pp. 4705-4712.
944 50. F. Wetscher, A. Vorhauer, R. Stock, and R. Pippan: *Mater. Sci. Eng. A*, 2004, vol. 387-389,
945   pp. 809-816.
946 51. C. Xu, Z. Horita, and T.G. Langdon: *Acta Mater.*, 2007, vol. 55, pp. 203-212.
947 52. C. Xu, Z. Horita, and T.G. Langdon: *Acta Mater.*, 2008, vol. 56, pp. 5168-5176.

948   53.   Y. Estrin, A. Molotnikov, C.H.J. Davies, and R. Lapovok: *J. Mech. Phys. Solids*, 2008, vol.
949   56, pp. 1186-1202.
950   54.   M. Kawasaki, R.B. Figueiredo, and T.G. Langdon: *Acta Mater.*, 2011, vol. 59, pp. 308-316.
951   55.   M. Kawasaki, B. Ahn, and T.G. Langdon: *Mater. Sci. Eng. A*, 2010, vol. A527, pp. 7008-
952   7016.
953   56.   M. Kawasaki: *J. Mater. Sci.*, 2014, vol. 49, pp. 18-34.
954   57.   J. Wongsa-Ngam and T.G. Langdon: *Mater. Sci. Forum*, 2014, vol. 783-786, pp. 2635-
955   2640.
956   58.   R.Z. Valiev and T.G. Langdon: *Adv. Eng. Mater.*, 2010, vol. 12, pp. 677-691.
957   59.   R.Z. Valiev and T.G. Langdon: *Metall. Mater. Trans. A*, 2011, vol. 42A, pp. 2942-2951.
958   60.   R.Z. Valiev, I. Sabirov, A.P. Zhilyaev, and T.G. Langdon: *JOM*, 2012, vol. 64, pp. 1134-
959   1142.
960   61.   K. Nakashima, Z. Horita, M. Nemoto, and T.G. Langdon: *Mater. Sci. Eng. A*, 2000, vol.
961   A281, pp. 82–87.
962   62.   G.I. Raab: *Mater. Sci. Eng. A*, 2005, vol. 410-411, pp. 230-233.
963   63.   M.Yu. Murashkin, E.V. Bobruk, A.R. Kil'mametov, and R.Z. Valiev: *Phys. Metals*
964   *Metallog.*, 2009, vol. 108, pp. 415-423.
965   64.   R.Z. Valiev, M.Yu. Murashkin, E.V. Bobruk, and G.I. Raab: *Mater. Trans.*, 2009, vol. 50,
966   pp. 87-91.
967   65.   I. Sabirov, M.T. Perez-Prado, M. Murashkin, J.M. Molina-Aldareguia, E.V. Bobruk, N.F.
968   Yunusova, and R.Z. Valiev: *Int. J. Mater. Form.*, 2010, vol. 3 (suppl. 1), pp. 411-414.
969   66.   D. Green: *J. Inst. Metals*, 1972, vol. 100, pp. 295-300.
970   67.   C. Etherington: *J. Eng. Ind.*, 1974, vol. 96, pp. 893-900.
971   68.   G.J. Raab, R.Z. Valiev, T.C. Lowe, and Y.T. Zhu: *Mater. Sci. Eng. A*, 2005, vol. A382, pp.
972   30-34.
973   69.   G.I. Raab, R.Z. Valiev, D.V. Gunderov, T.C. Lowe, A. Misra, and Y.T. Zhu: *Mater. Sci.*
974   *Forum*, 2008, vol. 584-586, pp. 80-85.
975   70.   S. Katsas, R. Dashwood, G. Todd, M. Jackson, and R. Grimes: *J. Mater. Sci.*, 2010, vol.
976   45, pp. 4188-4195.
977   71.   V.M. Segal: *J. Mater. Process. Tech.*, 2010, vol. 210, pp. 542-549.
978   72.   C. Xu, S. Schroeder, P.B. Berbon, and T.G. Langdon: *Acta Mater.*, 2010, vol. 58, pp. 1379-
979   1386.
980   73.   A.V. Polyakov, I.P. Semenova, G.I. Raab, V.D. Sitdikov, and R.Z. Valiev: *Rev. Adv.*
981   *Mater. Sci.*, 2012, vol. 31, pp. 78-84.
982   74.   I.P. Semenova, A.V. Polyakov, G.I. Raab, T.C. Lowe, and R.Z. Valiev: *J. Mater. Sci.*,
983   2012, vol. 47, pp. 7777-7781.
984   75.   D.V. Gunderov, A.V. Polyakov, I.P. Semenova, G.I. Raab, A.A. Churakova, E.I.
985   Gimaltdinova, I. Sabirov, J. Segurado, V.D. Sitdikov, I.V. Alexandrov, N.A. Enikeev, and
986   R.Z. Valiev: *Mater. Sci. Eng. A*, 2013, vol. A562, 128-136.
987   76.   J.T. Wang, Z. Li, J. Wang, and T.G. Langdon: *Scr. Mater.*, 2012, vol. 67, pp. 810-813.
988   77.   P.W. Bridgman: *J. Appl. Phys.*, 1943, vol. 14, pp. 273-283.
989   78.   Z. Li, P.F. Zhang, H. Yuan, K. Lin, Y. Liu, D.L. Yin, J.T. Wang, and T.G. Langdon:
990   *Mater. Sci. Eng. A*, 2016, vol. A658, pp. 367-375.
991   79.   T.H. Fang, W.L. Li, N.R. Tao, and K. Lu: *Science*, 2011, vol. 331, pp. 1587-1590.
992   80.   X. Wu, P. Jiang, L. Chen, F. Yuan, and Y.T. Zhu: *Proc. Natl. Acad. Sci. USA*, 2014, vol.
993   111, pp. 7197-7201.

994   81. K. Lu: *Science*, 2014, vol. 345, pp. 1455-1456.

995   82. W. Wang, F. Yuan, and X. Wu, *Comput. Mater. Sci.*, 2015, vol. 110, pp. 83-90.

996   83. A.V. Korznikov, I.M. Safarov, D.V. Laptionok, and R.Z. Valiev: *Acta Metall. Mater.*,
997   1991, vol. 39, pp. 3193-3197.

998   84. H. Shen, B. Guenther, A.V. Korznikov, and R.Z. Valiev: *Nanostruct. Mater.*, 1995, vol. 6,
999   pp. 385-388.

1000 85. R.Z. Valiev, R.S. Mishra, J. Groza, and A.K. Mukherjee: *Scr. Mater.*, 1996, vol. 34, pp.
1001   1443-1448.

1002 86. J. Sort, A.P. Zhilyaev, M. Zielinska, J. Nogues, S. Suriñach, J. Thibault, and M.D. Baró:
1003   *Acta Mater.*, 2003, vol. 51, pp. 6385-6393.

1004 87. Z. Lee, F. Zhou, R.Z. Valiev, E.J. Lavernia, and S.R. Nutt: *Scr. Mater.*, 2004, vol. 51, pp.
1005   209-214.

1006 88. K.V. Rajulapati, R.O. Scattergood, K.L. Murty, Z. Horita, T.G. Langdon, and C.C. Koch:
1007   *Metall. Mater. Trans. A*, 2008, vol. 39A, pp. 2528-2534.

1008 89. K. Kaneko, T. Hata, T. Tokunaga, and Z. Horita: *Mater. Trans.*, 2009, vol. 50, pp. 76-81.

1009 90. K. Edalati, Z. Horita, H. Fujiwara, and K. Ameyama: *Metall. Mater. Trans. A*, 2010, vol.
1010   A41, pp. 3308-3317.

1011 91. K. Edalati, S. Toh, M. Watanabe, and Z. Horita: *Acta Mater.*, 2012, vol. 60, pp. 3885-3893.

1012 92. K. Edalati, S. Toh, M. Watanabe, and Z. Horita: *Scr. Mater.*, 2012, vol. 66, pp. 386-389.

1013 93. K. Edalati, S. Toh, H. Iwaoka, M. Watanabe, Z. Horita, D. Dashioka, K. Kishida, and H.
1014   Inui: *Scr. Mater.*, 2012, vol. 67, pp. 814-817.

1015 94. J.M. Cubero-Sesin and Z. Horita: *Mater. Sci. Eng. A*, 2012, vol. A558, pp. 462-471.

1016 95. P. Jenei, J. Gibicza, E.Y. Yoon, and H.S. Kim: *J. Alloys Compd.*, 2012, vol. 539, pp. 32-36.

1017 96. E.Y. Yoon, D.J. Lee, T.S. Kim, H.J. Chae, P. Jenei, J. Gubicza, T. Ungár, M. Janecek, J.
1018   Vratna, S. Lee, and H.S. Kim: *J. Mater. Sci.*, 2012, vol. 47, pp. 7117-7123.

1019 97. A.P. Zhilyaev, G. Ringot, Y. Huang, J.M. Cabrera, and T.G. Langdon: *Mater. Sci. Eng. A*,
1020   2017 (in press).

1021 98. E. Menéndez, J. Sort, V. Langlais, A. Zhilyaev, J.S. Muñoz, S. Suriñach, J. Nogués, and
1022   M.D. Baró: *J. Alloys Compd.*, 2007, vol. 434-435, pp. 505-508.

1023 99. E. Menéndez, G. Salazar-Alvarez, A.P. Zhilyaev, S. Suriñach, M.D. Baró, J. Nogués, and J.
1024   Sort: *Adv. Funct. Mater.*, 2008, vol. 18, pp. 3293-3298.

1025 100. H. Li, A. Misra, Y. Zhu, C.C. Koch, and T.G. Holesinger: *Mater, Sci. Eng. A*, 2009, vol.
1026   A523, pp. 60-64.

1027 101. H. Li, A. Misra, Z. Horita, C.C. Koch, N.A. Mara, P.O. Dickerson, and Y. Zhu: *J. Appl.*
1028   *Phys.*, 2009, vol. 95, pp. 071907(1-4).

1029 102. A. Bachmaier, A. Hohenwarter, and R. Pippan: *Scr. Mater.*, 2009, vol. 61, 1016-1019.

1030 103. J. Sort, D.C. Ile, A.P. Zhilyaev, A. Concustell, T. Czeppe, M. Stoica, S. Suriñach, J. Eckert,
1031   and M.D. Baró: *Scr. Mater.*, 2004, vol. 50, pp. 1221-1225.

1032 104. A.R. Yavari, W.J. Botta, C.A.D. Rodrigues, C. Cardoso, and R.Z. Valiev: *Scr. Mater.*,
1033   2002, vol. 46, pp. 711-716.

1034 105. Z. Kovács, P. Henits, A.P. Zhilyaev, and A. Révész: *Scr. Mater.*, 2006, vol. 54, pp. 1733-
1035   1737.

1036 106. N. Boucharat, R. Hebert, H. Rösner, R.Z. Valiev, and G. Wilde: *J. Alloys Compds.,* 2007,
1037   vol. 434-435, pp. 252-254.

1038 107. T. Czeppe, G. Korznikova, J. Morgiel, A. Korznikov, N.Q. Chinh, P. Ochin, and A. Sypien
1039   *J. Alloys Compds.*, 2009, vol. 483, pp. 74-77.

1040 108. A.P. Zhilyaev, A.A. Gimazov, G.I. Raab, and T.G. Langdon: *Mater. Sci. Eng. A*, 2008, vol.
1041 A486, pp. 123-128.
1042 109. A.P. Zhilyaev, S. Swaminathan, A.A. Gimazov, T.R. McNelley, and T.G. Langdon: *J.
1043 Mater. Sci.*, 2008, vol. 43, pp. 7451-7456.
1044 110. K. Edalati, Y. Yokoyama, and Z. Horita: *Mater. Trans.*, 2010, vol. 51, pp. 23-26.
1045 111. K. Edalati and Z. Horita: *Scr. Mater.*, 2010, vol. 63, pp. 174-177.
1046 112. M.C. Chen, H.C. Hsieh, and W. Wu: *J. Alloys Compds.*, 2006, vol. 416, pp. 169-172.
1047 113. M.C. Chen, C.W. Kuo, C.M. Chang, C.C. Hsieh, Y.Y. Chang, and W. Wu: *Mater. Trans.*,
1048 2007, vol. 48, pp. 2595-2598.
1049 114. M. Eizadjou, A.K. Talachi, H.D. Manesh, H.S. Shahabi, and K. Janghorban: *Compos. Sci.
1050 Technol.*, 2008, vol. 68, pp. 2003-2009.
1051 115. R.N. Dehsorkhi, F. Qods, M. Tajally *Mater. Sci. Eng. A*, 2011, vol. A530, pp. 61-72.
1052 116. N. Chang, M.Y. Zheng, C. Xu, G.D. Fan, H.G. Brokmeier, and K. Wu: *Mater. Sci. Eng. A*,
1053 2012, vol. A543, pp. 249-256.
1054 117. B. Beausir, J. Scharnweber, J. Jaschinski, H.G. Brokmeier, C.G. Oertel, W. Skrotzki:
1055 *Mater. Sci. Eng. A*, 2010, vol. A527, pp. 3271-3278.
1056 118. K. Oh-ishi, K. Edalati, H.S. Kim, K. Hono, and Z. Horita: *Acta Mater.*, 2013, vol. 61, pp.
1057 3482-3489.
1058 119. O. Bouaziz, H.S. Kim, and Y. Estrin: *Adv. Eng. Mater.*, 2013, vol. 15, pp. 336-340.
1059 120. B. Ahn, A.P. Zhilyaev, H.J. Lee, M. Kawasaki, and T.G. Langdon: *Mater. Sci. Eng. A*,
1060 2015, vol. A635, pp. 109-117.
1061 121. M. Kawasaki, B. Ahn, H.J. Lee, A.P. Zhilyaev, and T.G. Langdon: *J. Mater. Res.*, 2016,
1062 vol. 31, pp. 88-99.
1063 122. B. Ahn, H.J. Lee, I.C. Choi, M. Kawasaki, J.I. Jang, and T.G. Langdon: *Adv. Eng. Mater.*,
1064 2016, vol. 18, pp. 1001-1008.
1065 123. M. Kawasaki, B. Ahn, P. Kumar, J.I. Jang, and T.G. Langdon: *Adv. Eng. Mater.*, 2017, vol.
1066 19, pp. 1600578(1-17).
1067 124. R.B. Figueiredo, P.R. Cetlin, and T.G. Langdon: *Mater. Sci. Eng. A*, 2011, vol. A528, pp.
1068 8198-8204.
1069 125. R.B. Figueiredo, P.H.R. Pereira, M.T.P. Aguilar, P.R. Cetlin, and T.G. Langdon: *Acta
1070 Mater.*, 2012, vol. 60, pp. 3190-3198.
1071 126. M. Kawasaki, S.N. Alhajeri, C. Xu, and T.G. Langdon: *Mater. Sci. Eng. A*, 2011, vol.
1072 A529, pp. 345-351.
1073 127. H.J. Lee, S.K. Lee, K.H. Jung, G.A. Lee, B. Ahn, M. Kawasaki, and T.G. Langdon: *Mater.
1074 Sci. Eng. A*, 2015, vol. A630, pp. 90-98.
1075 128. K. Lu: *Science*, 2010, vol. 328, pp. 319-320.
1076 129. R. Birringer: *Mater. Sci. Eng. A*, 1989, vol. A117, pp. 33-43.
1077 130. B. Gunther, A. Kumpmann, and H.-D. Kunze: *Scripta Metall. Mater.*1992, vol.27, pp. 833-
1078 838.
1079 131. M. Ames, J. Markmann, R. Karos, A. Michels, A. Tschope, and R. Birringer: *Acta Mater*.
1080 2008, vol. 56, pp. 4255-4266.
1081 132. F. J. Humphreys, and M. Hatherly: Recrystallization and Related Annealing Phenomena,
1082 chapter 9, (Elsevier Science, Inc., Tarrytown, NY, 1996), pp. 289-295.
1083 133. C. E. Krill, H. Ehrhardt, and R. Birringer: *Z. Metallkd.* 2005, vol. 96, pp. 1134-1141
1084 134. J. W. Cahn: *Acta Metallurgica*, 1962, vol.10, pp. 768-798.

1085 135. K. Lücke, and H. P. Stüwe: *Acta Metallurgica*, 1971, vol.19, pp. 1087-1099.

1086 136. P. Knauth, A. Charai, and P. Gas: *Scripta Metall. Mater.*, 1993, vol.28, pp. 325-330.

1087 137. A. Michels, C. E. Krill, H. Ehrhardt, R. Birringer, and D. T. Wu: *Acta Mater.*, 1999, vol.47,
1088   pp. 2143-2152.

1089 138. R. D. Doherty, *Mater. Sci. Forum*, 2012, vol. 715, pp. 1-12.

1090 139. R. J. Perez, H. G. Jiang, C. P. Dogan, and E. J. Lavernia: *Metall. Mater. Trans. A*, 1998,
1091   vol.29A, pp. 2469-2475.

1092 140. H. J. Hofler, and R. S. Averback: *Scripta Metall. Mater.*, 1990, vol. 24, pp. 2401-2406.

1093 141. Z. Gao, and G. Fultz: *NanoStructured Mater.*, 1994, vol. 4, pp. 939-947.

1094 142 Y. Estrin, G. Gottstein, E. Rabkin, and L. S. Shvindlerman: *Scripta Mater.*, 2000, vol. 43,
1095   pp. 141-147.

1096 143. E. D. Hondros, and M. P. Seah: in *Physical Metallurgy*, 3rd edition, ed. R. W. Cahn and P.
1097   Haasen, Elsevier Sci. Publ. BV, (1983) p. 856.

1098 144. J. Weissmuller: *NanoStructured Mater.*, 1993, vol. 3, pp. 261-272, & *J. Mater. Res.*, 1994,
1099   vol. 9, pp. 4-7.

1100 145. R. Kirchheim: *Acta Mater.*, 2002, vol. 50, pp. 413-419.

1101 146. J. R. Trelewicz, and C. A. Schuh: *Phys. Rev. B*, 2009, vol. 79, p. 094112.

1102 147. M. Saber, H. Kotan, C. C. Koch, and R. O. Scattergood: *J. Appl. Phys.*, 2013, vol. 113
1103   p. 063515.

1104 148. P. Wynblatt, and R. C. Ku: *Surf. Sci.* 1977, vol. 65, pp. 511-531.

1105 149. T. Chookajorn, H. A. Murdoch, and C. A. Schuh: *Science*, 2012, vol. 337, pp. 951-954.

1106 150. A. R. Kalidindi, T. Chookajorn, and C. A. Schuh: *JOM,* 2015, vol. 67, pp. 2834-2843.

1107 151. S. J. Dillon, M. Tang, W. C. Carter, and M. P. Harmer: *Acta Mater.,* 2007, vol. 55, pp.
1108   6208-6218.

1109 152. T. J. Rupert: *Current Opinion in Solid State and Mater. Sci.*, 2016, vol. 20, pp. 257-267.

1110 153. A. Khalajhedayati, and T. J. Rupert: *JOM,* 2015, vol. 67, pp. 2788-2801.

1111 154. M. Saber, H. Kotan, C. C. Koch, and R. O. Scattergood: *Mater. Sci. Engr. A*, 2012, vol.
1112   556, pp. 664-670.

1113 155. L. Li, M. Saber, W. Xu, Y. Zhu, C. C. Koch, and R.O. Scattergood: *Mater. Sci. Engr. A*,
1114   2014, vol. 613, pp. 289–295.

1115 156. M. Saber, H. Kotan, C. C. Koch, and R.O. Scattergood: *J. Appl. Phys.*, 2013, vol.114, p.
1116   103510.

1117 157. E.J. Lavernia, B.Q. Han, and J.M. Schoenung: *Mater. Sci. Eng. A,* 2008, vol. 493, pp. 207-
1118   214.

1119 158. H.J. Fecht: *Nanophase Materials: Synthesis, Properties, Applications*, in: G.C.
1120   Hadjipanayis, R.W. Siegel (Eds.), Kluwer Academic, Dordrecht, Netherlands, 1994.

1121 159. D.B. Witkin, and E.J. Lavernia: *Prog. Mater. Sci.*, 2006, vol. 51, pp. 1-60.

1122 160. J.A. Picas, A. Forn, L. Ajdelsztajn, and J. Schoenung: *Powder Tech.*, 2004, vol. 148, pp.
1123   20-23.

1124 161. B. Huang, R.J. Perez, and E.J. Lavernia: *Mater. Sci. Eng. A*, 1998, vol. 255, pp. 124-132.

1125 162. O. Ertorer, T. Topping, Y. Li, W. Moss, and E.J. Lavernia: *Scripta Mater.*, 2009, vol. 60,
1126   pp. 586-589.

163. X. Zhang, H. Wang, R.O. Scattergood, J. Narayan, and C.C. Koch: *Acta Mater.*, 2002, vol. 50, pp. 3995-4004.

164. B. Zheng, O. Ertorer, Y. Li, Y. Zhou, S. N. Mathaudhu, C. Y.A. Tsao, and E.J. Lavernia: *Mater. Sci. Eng. A*, 2011, vol. 528, pp. 2180-2191.

165. B. Zheng , Y. Li , W. Xu , Y. Zhou , S.N. Mathaudhu , Y. Zhu, and E.J. Lavernia, *Phil. Mag. Lett.*, 2013, vol. 93, pp. 457-464.

166. N. Yang, J.K. Yee, Z. Zhang, L. Kurmanaeva, P. Cappillino, V. Stavila, E.J. Lavernia, and C. San Marchi: *Acta Mater.*, 2015, vol. 82, pp. 41-50.

167. K.M. Youssef, A.J. Zaddach, C. Niu, D.L. Irving, and C.C. Koch: *Mater. Res. Lett.*, 2015, vol. 3, pp. 95-99.

168. B. Zheng, Z. Fu, L. Kurmanaeva, Y. Lin, J. Ivanisenko, Y. Zhou, F. Chen, H. Hahn, L. Zhang, and E.J. Lavernia: *TMS2016*, Nashville TN, 2016.

169. J. Ye, J. He, and J.M. Schoenung: *Metall. Mater. Trans. A*, 2006, vol. 37, pp. 3099-3109.

170. F. Tang, M. Hagiwara, and J.M. Schoenung: *Scripta Mater.*, 2005, vol. 53, pp. 619-624.

171. H.-J. Fecht: *Nanostruct. Mater.*, 1995, vol. 6, pp. 33-42.

172. F. Zhou, X.Z. Liao, Y.T. Zhu, S. Dallek, and E.J. Lavernia: *Acta Mater.*, 2003, vol. 51, pp. 2777-2791.

173. X.Z. Liao, J.Y. Huang, Y.T. Zhu, F. Zhou, and E.J. Lavernia: *Phil. Mag.*, 2003, vol. A83, pp. 3065-3075.

174. J. Eckert, J.C. Holzer, C.E. Krill III, and W.L. Johnson: *J. Mater. Res.*, 1992, vol. 7, pp. 1751-1761.

175. F.A. Mohamed: *Acta Mater.*, 2003, vol. 51, pp. 4107-4119.

176. B. Zheng, D. Zhang, Y. Zhou, S.N. Mathaudhu, and E.J. Lavernia: in D.C.a.R.M. Gasior (Ed.) *Adv. in Powder Metall. & Particulate Mater. 2013*, Metal Powder Industries Federation, Chicago, IL, 2013.

177. D.T.A. Matthews, V. Ocelík, P.M. Bronsveld, and J.T.M. De Hosson: *Acta Mater.*, 2008, vol. 56, pp. 1762-1773.

178. K. Hajlaoui, A.R. Yavari, B. Doisneau, A. LeMoulec, W.J. Botta F,G. Vaughan, A.L. Greer, A. Inoue, W. Zhang, and Å. Kvick: *Scripta Mater.*, 2006, vol. 54, pp. 1829-1834.

179. X. Zhang, H. Wang, and C.C. Koch: *Rev. Adv. Mater. Sci.*, 2004, vol. 6, pp. 53-93.

180. K.H. Chung, D.H.S. J. He, and J.M. Schoenung: *Mater. Sci. Eng. A*, 2003, vol. 356, pp. 23-31.

181. R. Vogt, Z. Zhang, Y. Li, M. Bonds, N.D. Browning, E.J. Lavernia, and J.M. Schoenung: *Scripta Mater.*, 2009, vol. 61, pp. 1052-1055.

182. C.C. Koch: in H. R.W. Siegel , M.C. Roco (Ed.) Final report by WTEC panel, 1999, pp. 93.

183. Y.T. Zhu, and X. Liao: *Nature Mater.*, 2004, vol. 3, pp. 351-352.

184. L. Lu, Y.F. Shen, X.H. Chen, L.H. Qian, and K. Lu: *Science*, 2004, vol. 304, pp. 422-426.

185. Y.H. Zhao, J.F. Bingert, X.Z. Liao, B.Z. Cui, K. Han, A.V. Sergueeva, A.K. Mukherjee, R.Z. Valiev, T.G. Langdon, and Y.T. Zhu: *Adv. Mater.*, 2006, vol. 18, pp. 2949-2953.

186. K. Lu, *Nature Rev. Mater.*, 2016, vol. 1, #16019, pp. 1-13.

187. L. Lu, Y.F. Shen, X.H. Chen, L.H. Qian, and K. Lu: *Science*, 2004, vol. 304, pp. 422-426.

188 M.A. Meyers, O. Vohringer, and V.A. Lubarda: *Acta Mater.*, 2001, vol. 49, pp. 4025-4039.

189. M.A. Meyers, A. Mishra, and D.J. Benson: *Prog. Mater. Sci.*, 2006, vol. 51, pp. 427-556.

190. E. El-Danaf, S.R. Kalidindi, and R.D. Doherty: *Metall. Mater. Trans. A*, 1999, vol. 30, pp. 1223-1233.
191. Y.T. Zhu, X.Z. Liao, and X.L. Wu: *Prog. Mater. Sci.*, 2012, vol. 57, pp. 1-62.
192. B. Zheng , Y. Li , W. Xu , Y. Zhou , S.N. Mathaudhu , Y. Zhu, and E.J. Lavernia, Phil. Mag. Let., 2013, vol. 93, pp. 457-464.
193. J. He, K.H. Chung, X.Z. Liao, Y.T. Zhu, and E.J. Lavernia: *Metall. Mater. Trans. A*, 2003, vol. 34A, pp. 707-712.
194. S. Mahajan, and G.Y. Chin: *Acta Mater*, 1973, vol. 21, pp. 1353-1363.
195. W.B. Jones, and H.I. Dawson: in R.W. Rohde, B.M. Butcher, J.R. Holland, C.H. Karnes (Eds.) *Metallurgical Effects at High Strain Rates*, Plenum Press, New York, NY,, 1973, pp. 443-459.
196. V. Yamakov, D. Wolf, S.R. Phillpot, A.K. Mukherjee, and H. Gleiter: *Nature Mater.*, 2002, vol. 1, pp. 45-49.
197. J.A. Venables: in R.E. Reed-Hill, J. P. Hirth, H.C. Rogers (Eds.) *Deformation Twinning*, Gordon & Breach, NY, 1964, pp. 77-116.
198. K.W. Jacobsen, and J. Schiøtz: *Nature Mater.*, 2002, vol. 1, pp. 15-16.
199. Y. Wang, L.Q. Chen, Z.K. Liu, and S.N. Mathaudhu: *Scripta Mater.*, 2010, vol. 62, pp. 646-649.
200. H. Somekawa, K. Hirai, H. Watanabe, Y. Takigawa, and K. Higashi: *Mater. Sci. Eng. A*, 2005, vol. 407, pp. 53-61.
201. F. Zhou, X.Z. Liao, Y.T. Zhu, S. Dallek, and E.J. Lavernia: *Acta Mater.*, 2003, vol. 51, pp. 2777-2791.
202. F. Louchet, L.P. Kubin, and D. Vesely: *Phil. Mag. A*, 1979, vol. 39, pp. 433-454.
203. J.L. Sun, P.W. Trimby, X. Si, X.Z. Liao, N.R. Tao, and J.T. Wang: *Scripta Mater.*, 2013, vol. 68, pp. 475-478.
204. J.W. Christian, and S. Mahajant: *Prog. Mater. Sci.*, 1995, vol. 39, pp. 1-157.
205. X.L. Wu, K.M. Youssef, C.C. Koch, S.N. Mathaudhu, L.J. Kecskes, and Y.T. Zhu: *Scripta Mater.*, 2011, vol. 64, pp. 213-216.
206. M. Pozuelo, C. Melnyk, W.H. Kao, and J.-M. Yang: *J. Mater. Res.*, 2011, vol. 26, pp. 904-911.
207. Y. Li, Y.J. Lin, Y.H. Xiong, J.M. Schoenung, and E.J. Lavernia: *Scripta Mater.*, 2011, vol. 64, pp. 133-136.
208. S.N. Mathaudhu, J. Taek-Im, R.E. Barber, I.E. Anderson, I. Karaman, K.T. Hartwig, *Mater. Res. Soc. Symp. Proc.*, 2003, vol. 754, pp. CC3.5.1-8.
209. Y. Lin, and E.J. Lavernia: *Metall. Mater. Trans. A*, 2006, vol. 37, pp. 3317-3322.
210. H. Wen, Y.H. Zhao, Y. Li, O. Ertorer, K.M. Nesterov, R.K. Islamgaliev, R.Z. Valiev, and E.J. Lavernia: *Phil. Mag.*, 2010, vol. 90, pp. 4541-4550.
211. Y. Li, Y. H. Zhao, W. Liu, Z. H. Zhang, R. G. Vogt, E. J. Lavernia, and J.M. Schoenung: *Phil. Mag.*, 2010, vol. 90, pp. 783-792.
212. C.C. Koch, *J. Mater. Sci.*, 2007, vol. 42, pp. 1403-1414.
213. C. Koch, R. Scattergood, K. Darling, and J. Semones: *J. Mater. Sci.*, 2008, vol. 43, pp. 7264-7272.
214. P.V. Liddicoat, X. Liao, Y. Zhao, Y. Zhu, M.Y. Murashkin, E.J. Lavernia, R.Z. Valiev, and S.P. Ringer: *Nature Commun.*, 2010, vol. 7, pp. 1-7.
215. N. Zhou, T. Hu, J. Huang, and J. Luo: *Scripta Mater.*, 2016, vol. 124, pp. 160-163.

1217 216. Y. Lin, H. Wen, Y. Li, B. Wen, W. Liu, and E.J. Lavernia: *Acta Mater.*, 2015, vol. 82, pp.
1218   304-315.
1219 217. B.J.M. Aikin, R.M. Dickerson, D.T. Jayne, S. Farmer, and J.D. Whittenberger: *Scripta*
1220   *Metall. Mater.*, 1994, vol. 30, pp. 119-122.
1221 218. R.W. Hayes, P.B. Berbon, and R.S. Mishra: *Metall. Mater. Trans. A,* 2004, vol. 35, pp.
1222   3855-3861.
1223 219. Y. Li, W. Liu, V. Ortalan, W.F. Li, Z. Zhang, R. Vogt, N.D. Browning, E.J. Lavernia, and
1224   J.M. Schoenung: *Acta Mater.*, 2010, vol. 58, pp. 1732-1740.
1225 220. F. Zhou, J. Lee, S. Dallek, and E.J. Lavernia: *J. Mater. Res.*, 2001, vol. 16, pp. 3451-3458.
1226 221. I. Roy, M. Chauhan, F.A. Mohamed, and E.J. Lavernia: *Metall. Mater. Trans. A*, 2006, vol.
1227   37, pp. 721–730.
1228 222. B.Q. Han, Z. Zhang, and E.J. Lavernia: *Phil. Mag. Lett.*, 2005, vol. 85, pp. 97-108.
1229 223. V.L.Tellkamp, A. Melmed, and E.J. Lavernia: *Metall. Mater.Trans. A*, 2001, vol. 32, pp.
1230   2335-2345.
1231 224. J.E. Burke: Trans.TMS-AIME, 1949, vol. 180, pp. 73-79.
1232 225. A.P. Newbery, S.R. Nutt, and E.J. Lavernia: *JOM*, 2006, vol. 58, pp. 56-61.
1233 226. E. Kuş, Z. Lee, S. Nutt, and F. Mansfeld: *Corrosion*, 2006, vol. 62, pp. 152-154.

1234

1235

1236

1237

1238

1239 **Figure Captions.**

1240

1241 Fig. 1 OIM images for high purity aluminum in (a) the initial unprocessed condition and after
1242   ECAP through (b) 1, (c) 2, (d) 3, (e) 4, (f) 8 and (g) 12 passes using route B_C at RT: the
1243   grain colors correspond to the orientations in the unit triangle [44].

1244 Fig. 2 EBSD orientation images of Cu-0.1% Zr disks processed by HPT for (a) 1/4
1245 turn, (b) 5 turns and (c) 10 turns: the columns display images from the center of the
1246 disk (on left) and at the edge of the disk (on right) [57].

1247 Fig. 3 Schematic illustration of the principle of the ECAP–Conform process [72].

1248 Fig. 4 Multilayered structure with alternate distribution of finer and coarser grains fabricated by
1249   an ABAB-type 5N-Al/4N-Al bimetallic tube with 2 turns of t-HPS at RT: the 4NAl layers
1250   have finer grain size(<1 μm) and the 5N Al layers have relatively coarser grains [78].

1251 Fig. 5 Color-coded contour maps of the Vickers microhardness for the Al/Mg system after HPT
1252   for 1 turn (upper), 5 turns (center) and 10 turns (lower): the values associated with the
1253   various colors are given in the hardness color key on the right [120].

1254 Fig. 6 The range of fracture toughness and strength-to-weight ratio for many metals and
1255   materials [128] where the synthesized Al-Mg system shown in Fig. 5 after HPT is
1256   incorporated into the diagram as HPT-induced aluminum MMNCs without delineating
1257   any upper limits for these values [122].

1258 Fig.7: Model predictions of (a) grain size, and (b) interfacial solute excess for Fe-Zr alloys
1259   [147].

1260 Fig. 8: The nanostructure stability map for tungsten-based alloys at 1373 K (1100°C), calculated
1261   on the basis of variation of the enthalpy parameters. For each combination of parameters,
1262   the free energy of nanocrystalline structures is compared to that of the bulk regular
1263   solution. An example for the nanocrystalline stable region in given in (B) for W-Sc. A
1264   bulk stable case is given in (C) for W-Ag. (Reproduced with permission from reference
1265   [149]).

1266 Fig. 9. Bright field grain size histogram for Fe – 10 at.% Cr – 2 at.% Zr sample annealed at
1267   1173K (900˚C) [154].

1268 Fig. 10. Figure 10. Hall-Petch plot of Fe – 14Cr – 4Hf alloy along with the base Fe – 14Cr alloy
1269   [155].

1270 Fig. 11. Model prediction for Fe – 14Cr – x Hf alloys for grain size [156].Fig. 12: Literature
1271   data for thermal stabilization mechanisms vs. maximum homologous temperature for
1272   stabilization.

1273 Fig. 12. Figure 12. Literature data for thermal stabilization mechanisms vs. maximum
1274   homologous temperature for stabilization [156]. The symbols are: thermodynamic
1275   stabilization: ●, kinetic stabilization: ○, kinetic and thermodynamic stabilization: ▼,
1276   kinetic and complexion stabilization: Δ

1277 Fig. 13: Comparison of the average grain size evolution with milling time for Zn powder milled
1278   at room temperature and at liquid nitrogen temperature [179].

1279 Fig. 14: HREM image of Al-7.5Mg alloy cryomilled for 8 h, (a) Image of a whole nanoscale
1280   twin. (b) Local magnification of a twin [193].
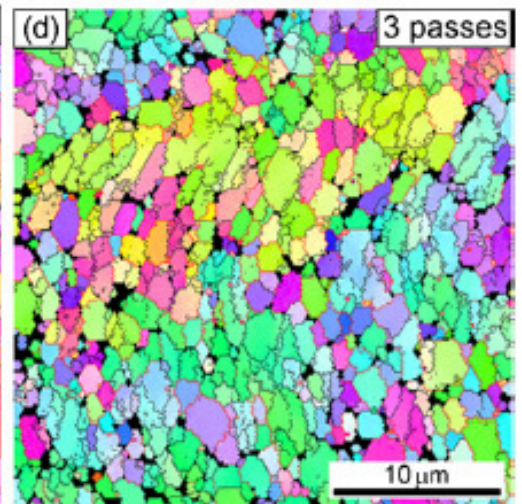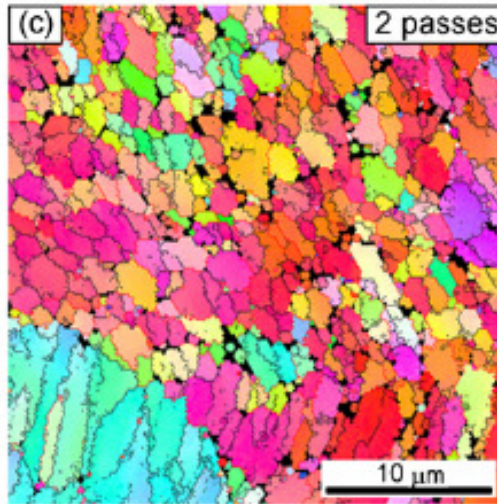
1281

1282

1283
1284
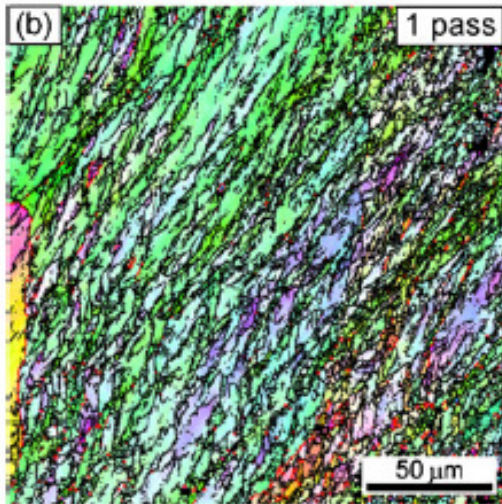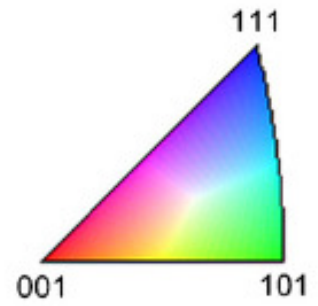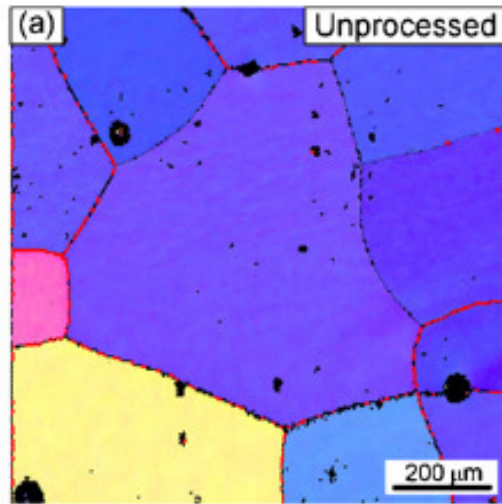1285
1286
1287

1288

1289

Article File with Track Changes.

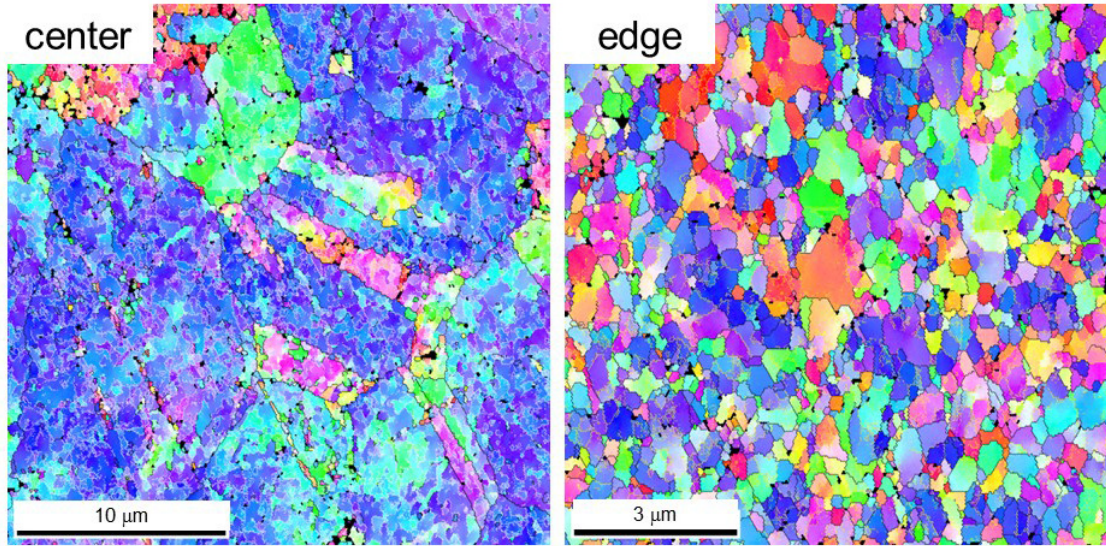As per the Response Letter, we have not made any changes in the original manuscript.

C. C. Koch, T. G. Langdon, E. J. Lavernia

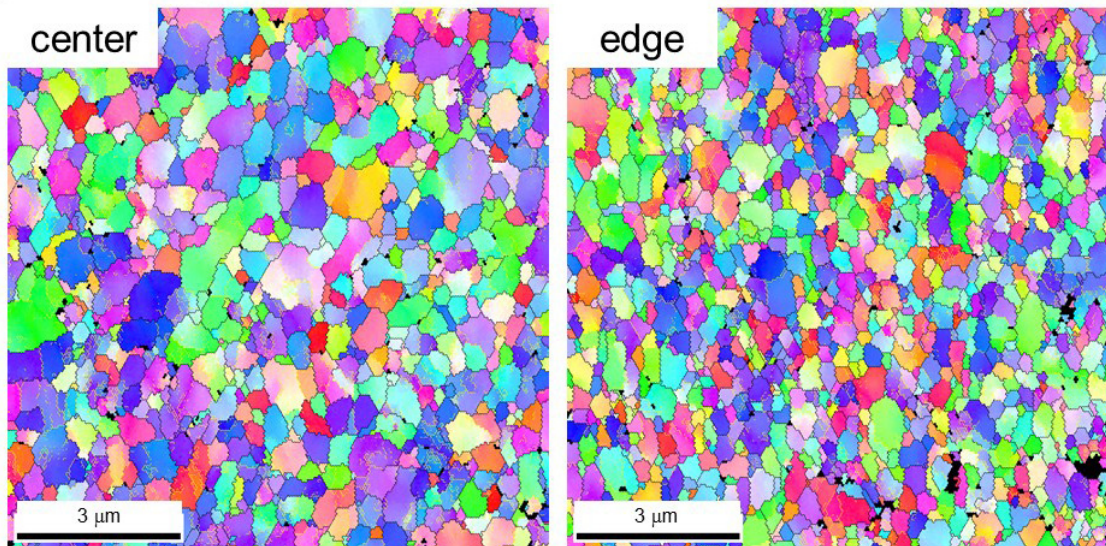(a) Unprocessed — 200 μm

2-15° (black)
>15° (red)

111
001   101

(b) 1 pass — 50 μm
(c) 2 passes — 10 μm
(d) 3 passes — 10 μm
(e) 4 passes — 10 μm
(f) 8 passes — 10 μm
(g) 12 passes — 2 μm
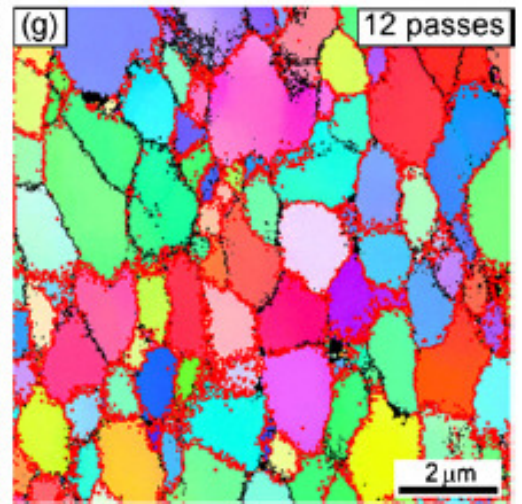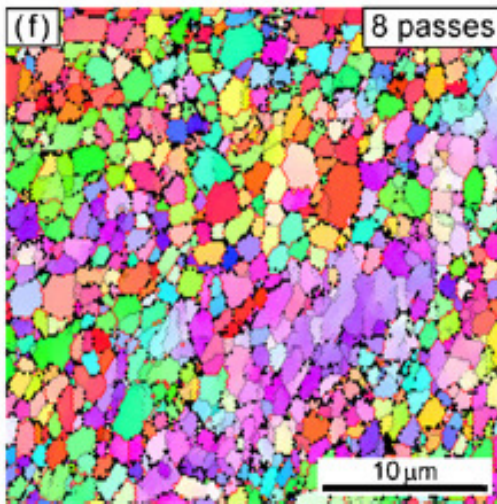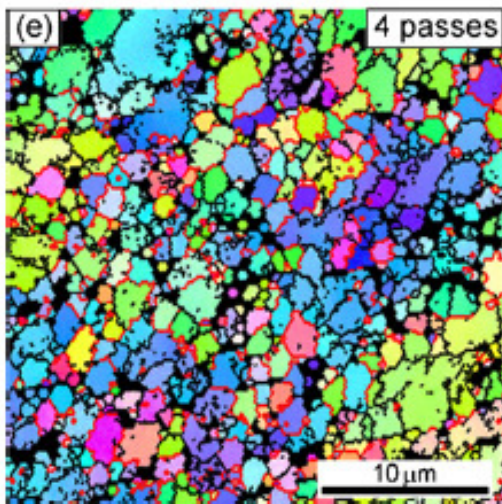
Cu-0.1 wt.% Zr
HPT: 6.0 GPa, RT

N = 1/4 turn

center

10 µm

edge

3 µm

(a)

N = 5 turns

center

3 µm

edge

3 µm

(b)

N = 10 turns

center

3 µm

edge

3 µm

(c)

Stationary die constructed from steel

Internal channel

30 cm

3.5 mm

Abrupt abutment to displace sample through $\Phi = 90°$

12 cm

Φ

30 cm

Exit channel

Rotating inner shaft

rectangular cross-section

4.0 mm

Entrance channel

transition from circular to rectangular cross-section

circular cross-section

4N-Al

5N-Al

ABAB type

SD

200 μm

EBSD area

AD

NSP

111

001

101

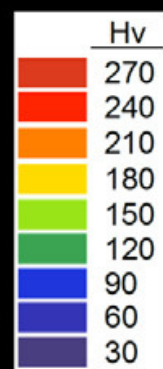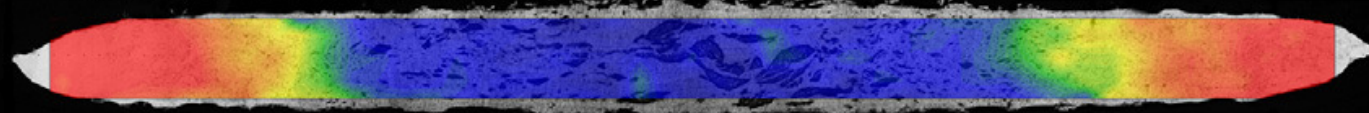t-HPS 2 turns: 4N/5N Al multilayered structure

SD

50μm

AD

NSP
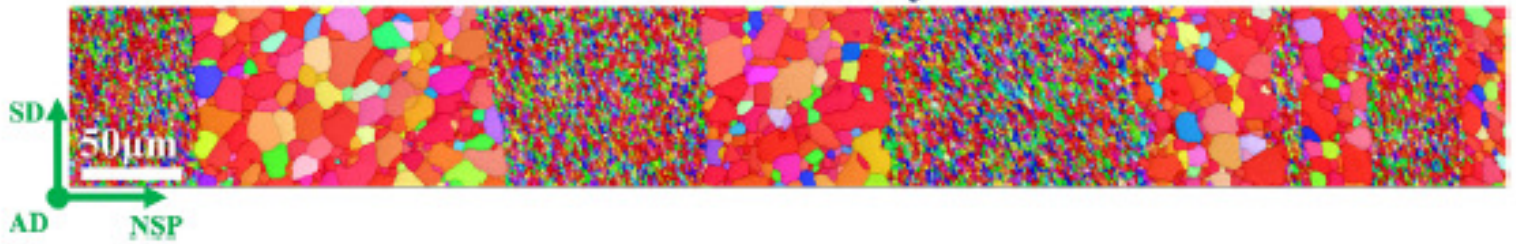
HPT: 1 turn, 6.0 GPa, RT, 1 rpm
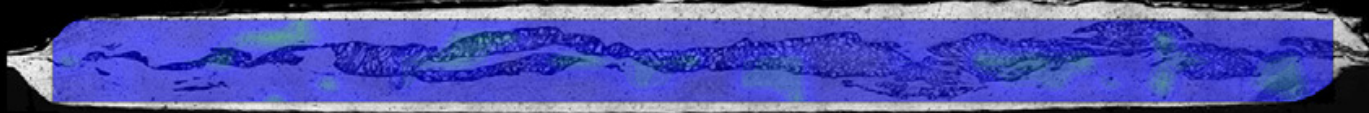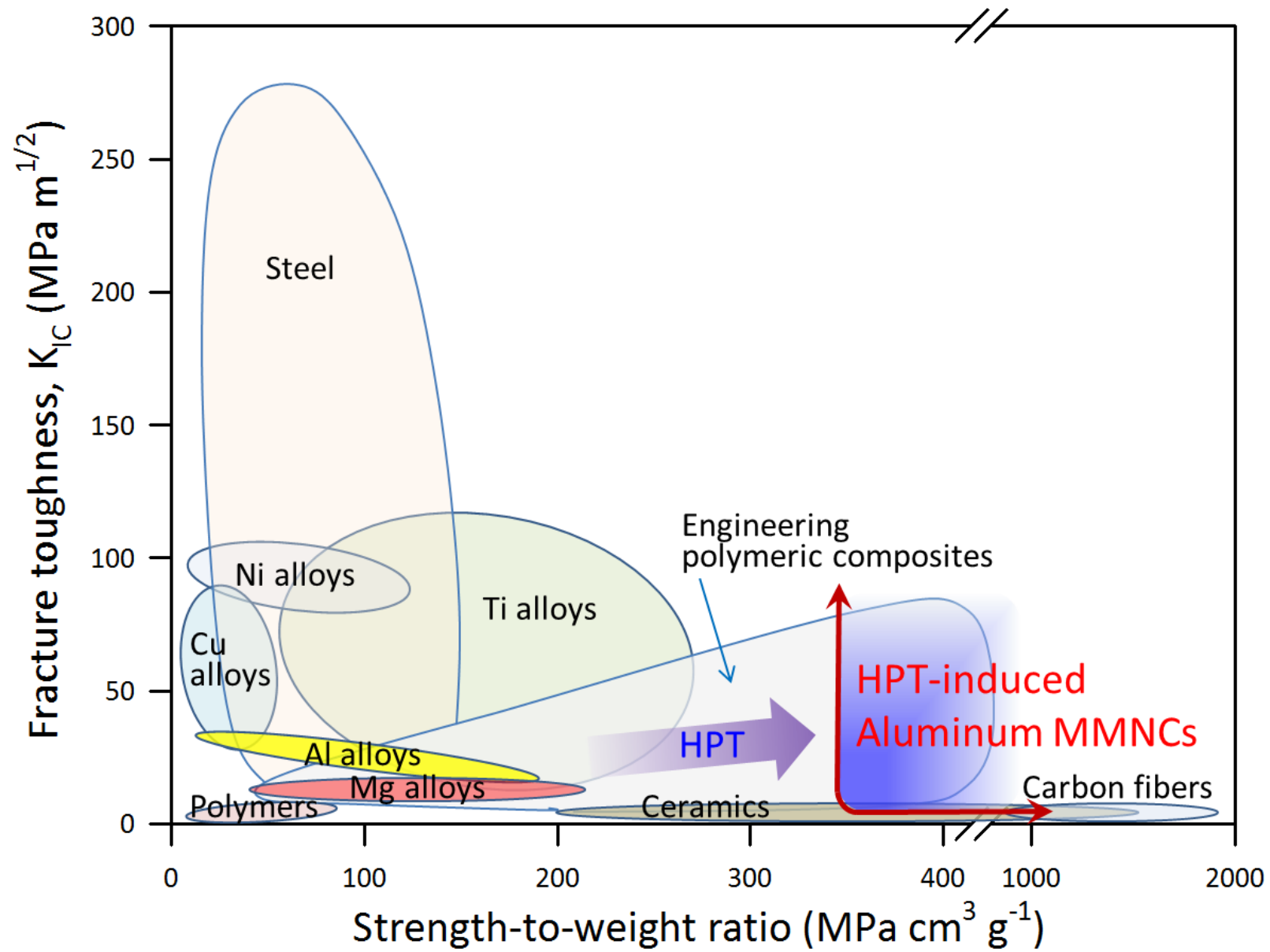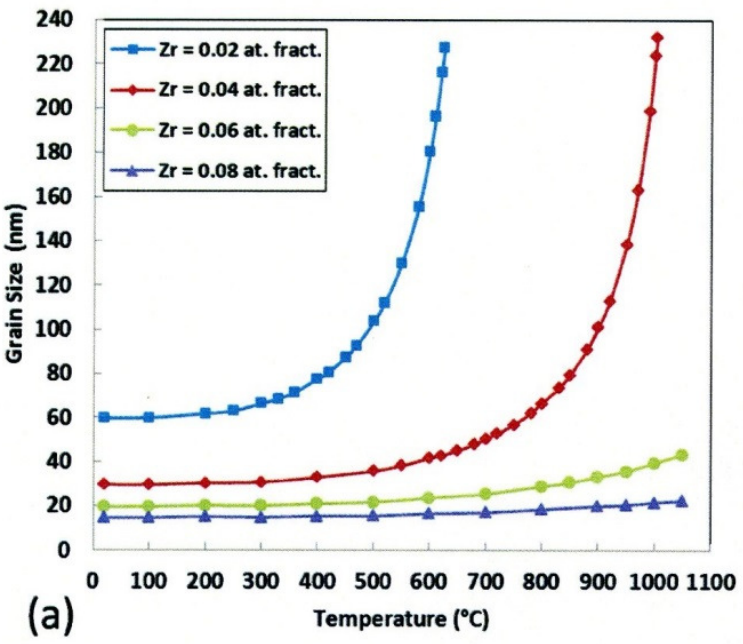
HPT: 5 turns, 6.0 GPa, RT, 1 rpm

HPT: 10 turns, 6.0 GPa, RT, 1 rpm

Hv

270
240
210
180
150
120
90
60
30

1 mm

(a)

(b)

A — Nanocrystalline stable / Bulk stable phase map at 1100 °C, with axes Enthalpy of Segregation (kJ/mol) versus Enthalpy of Mixing (kJ/mol), showing elements Th, In, Sc, Cu, Cd, Sr, Ag, Mn, Zn, Au, Cr, and Ti.

B — Free Energy versus Global Composition, Nanostructures, W-Sc Stable.

C — Free Energy versus Global Composition, Nanostructures, W-Ag Not Stable.

$[1\bar{1}2]$ ►